Techniques for Discovering and Identifying New Elements

M. Sc. Thesis
Johan Jeppsson

DIVISION OF NUCLEAR PHYSICS
LUNDS TEKNISKA HÖGSKOLA

Supervisors: Pavel Golubev and Dirk Rudolph

January 19, 2012

LUNDS UNIVERSITET
Lunds Tekniska Högskola

Abstract

This thesis deals primarily with the technical aspects of an upcoming nuclear physics experiment, which attempts to identify the super-heavy element 115 through X-ray fingerprinting. A general background of the different parts involved in running a super-heavy experiment with the TASCA separator at the GSI Helmholtzzentrum für Schwerionenforschung is covered, specifically focusing on experiments using the TASISpec detector set-up developed in Lund. In preparation for the element 115 experiment, two upgrades were made to TASISpec: the single-sided silicon strip detectors were exchanged to double-sided silicon strip detectors, and new analogue-to-digital converters (ADCs) were used. These modifications will be covered, including a dead layer correction that is made possible by the new detectors. An investigation of the resolution settings of the new ADCs is briefly described. Finally, the development and functionality of a "beam shut-off" routine to be used during the element 115 experiment will be described, as well as the upgraded version used for the element 120 experiment.

Contents

Acknowledgements

I would like to thank my supervisors, Dirk and Pavel, for giving me the opportunity to experience all the different aspects involved in running a modern nuclear physics experiment, and for putting up with all the questions from a nuclear novice as myself. I have found the experience immensely interesting and rewarding. I would also like to thank Ulrika for helping me throughout my time with the group, and Pico who provided a lot of valuable insight regarding the software aspects of data acquisition and data sorting using GO4.

Thanks also to all the nice people at GSI who always took time to explain the workings of the impressive machinery that make up TASCA and the UNILAC. It has been akin to walking around a toy shop for an engineer.

Finally, I would like to express my gratitude to my family for supporting me throughout my endeavours. Although I might not have expressed it often enough, it has been greatly appreciated.

1 Introduction

> *It would be a poor thing to be an atom in a universe without physicists, and physicists are made of atoms. A physicist is an atom's way of knowing about atoms.*
>
> George Wald (1906-1997)
> Nobel laureate in Physiology/Medicine 1967

MANKINDS QUEST IN UNDERSTANDING THE WORLD dates back millennia. The question "*what is everything made of?*" is a fundamental one, and one which has been answered in different ways by the great scientific minds throughout history.

In the 5th century BC, greek philosopher Democritus would have said that world around us is made up of minuscule indivisible particles of matter, called *atoms*, separated by void. If you asked Plato (428–348 BC), he would tell you that everything is made up of four fundamental elements: earth, water, air and fire (today referred to as *classical elements*), each represented by a platonic solid. It is said that he disliked the ideas of Democritus so immensely that he wished for all his books to be burned. Since they were already in such wide circulation, he instead resorted to never mentioning Democritus in his works.

A later student of Plato's academy, Aristotle (384-322 BC), added a fifth element, Aether, which made up the heavens and the stars. He claimed these elements were continuous, rather than made up of small particles. Due to the large impact of Aristotle's ideas on western philosophy, the idea of atoms was eclipsed and largely ignored for almost two millennia.

A theory much like atomism, called corpuscularianism, became prevalent in the 17th century, with proponents such as Rene Descartes, Robert Boyle, and John Locke. Here all mater is thought to be made up from small corpuscles, but their indivisibility is not expressively stated in the way it was for Democritus' atoms. So far, however, atoms and corpuscles had only been philosophical concepts, without any empirical backing.

The first truly scientific theory of the atom was put forward by John Dalton in the early 19th century. He claimed that all elements were made up of atoms which could not be created or destroyed and that chemical reactions were the combination, separation and rearrangement of these atoms. This was supported by the fact that if two elements react to form more than one compound, the masses of the two elements will combine in ratios of small numbers, suggesting that one reaction corresponds to m atoms of the first element reacting with n atoms of the second, where m and n are small positive integers. For instance, carbon and oxygen can form two compounds. In one, the mass ratio of the consumption of the two elements is 3:4; in the other it is 3:8. This can be interpreted as one carbon atom reacting with one oxygen atom in the first case, to form CO, or two in the second case, to form CO_2.

For close to a century atoms were thought to be an indivisible unit, until the discovery of the negatively charged *electron* by J. J. Thomson in 1897, which he claimed to be a constituent of the atom, and Rutherford's discovery in 1909 of the fact that most of the atom's mass is concentrated to the center. This formed the basis of the atomic model, put forward by Rutherford, of an atom consisting of a small positively charged nucleus in the center of the atom, surrounded by electrons.

It was later discovered that elements with the same nuclear charge could have different masses. It was eventually understood that the charge of the nucleus was decided by the number of positively charged particles, called *protons*, and these variations in mass, known as *isotopes*, was due to different numbers of electrically neutral particles, called *neutrons*, in the nucleus. Thus the basic building blocks used in nuclear physics were put in place.

Most of the elements up to uranium, with its 92 protons, were discovered in nature over the years. A handful exceptions include technetium (43 protons), promethium (61 protons), as well as some of the elements with a few protons less than uranium. These ”missing” elements, as well as all the elements with more protons than uranium, called *transuranic* elements, are unstable and have a half-life (the time it takes for half of the atoms to decay) much shorter than the age of the earth, which is why they have not been found in nature. During the 1940s, the periodic table began to expand, as transuranic elements started to be produced synthetically in laboratories using nuclear reactions. Since then increasingly heavier elements have been produced at a rather steady pace by bombarding heavy elements with particle beams of various lighter elements.

Appropriately, the very heaviest elements are referred to as *super-heavy elements* (SHE). However, no universal definition of where the division between super-heavy and simply heavy lies exists; some call all transuranic elements super-heavy, while others only consider elements with 100 or more protons to be sufficiently heavy [1]. Definitional ambiguities aside, the research of super-heavy elements is a hot topic in present day nuclear physics.

Today, all elements up to number 112, as well as 114 and 116 have been discovered and the respective discovery claims approved by the International Union of Pure and Applied Chemistry (IUPAC), which is considered the world authority for naming elements; claims for elements 113, 115, 117 and 118 have been put forward, but are as of yet not approved. The last to be discovered, element 117, was added to the list in April 2010 [3], thereby completing the sequence of discovered proton numbers from 1 to 118. Figure 1 shows the chart of nuclides, where all the discovered elements are organized according to their proton and neutron number.

The credit for the discovery of new elements is of course prestigious, which is evident from the names given to them. These include Darmstadtium, named after Darmstadt where the GSI institute behind the discovery is located, and Dubnium, named after Dubna in Russia where it was discovered. Famous scientists have also been a common basis for new names. Recently, Swedish chemists have been lobbying for the name ”berzelium” [4] to be adopted for one of the yet unnamed elements in honour of the Swedish chemist Jöns Jacob Berzelius, who is considered to be one of the fathers of modern chemistry. They are criticising previous names for ignoring chemists and being too focused on famous physicists.

As nuclei become heavier, they not only become more difficult to produce; they also become increasingly short lived, decaying in thousands, or even millionths, of a second. When looking at the stability of existing nuclei, certain numbers show up repeatedly in the proton and neutron numbers of nuclei that are especially stable compared to neighbouring isotopes. These, so called *magic numbers*, illustrated in figure 1, are an interesting aspect of nuclear structure,

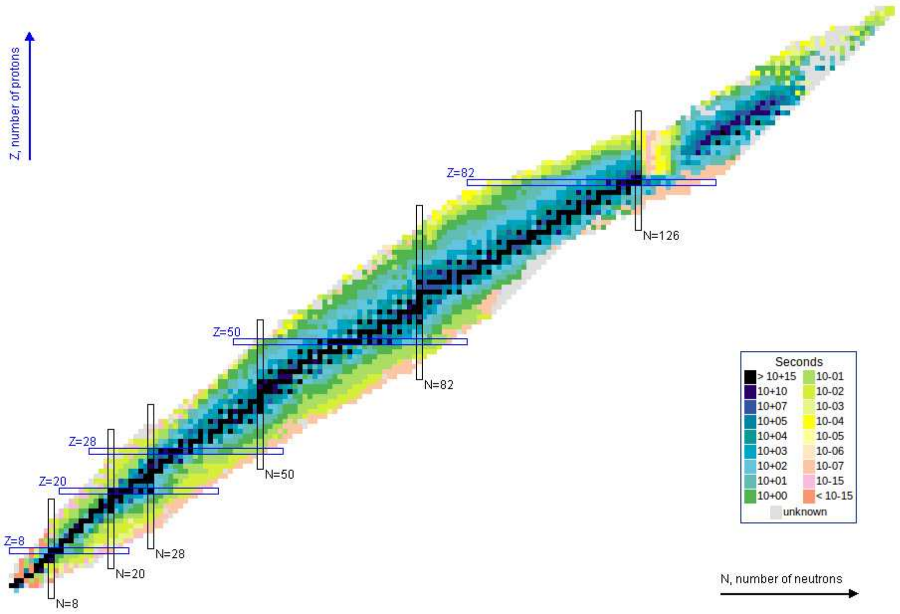

Figure 1: The chart of nuclides. The number of protons increase along the vertical axis and the number of neutrons along the horizontal axis. Black elements are stable; the other colors represent different half-lives, as illustrated by the legend on the right. Magic numbers are indicated with vertical and horizontal strips. Taken from Ref. [2].

as they indicate that certain numbers of nucleons can be arranged in a more stable configuration than others.

This lead physicist Glenn T. Seaborg to speculate on the possibility of the existence of elements with relatively long half-lives compared to the other super-heavy elements at the top right of the chart of nuclides. This theorized area, known as the *island of stability*, is one of the most interesting aspects of super-heavy element research today, as it could provide valuable insight of the nuclear structure of these exotic elements. The discovery of the most recent elements are expected to lie on the south-west shore of this area. The longest half-lives are expected on the south-east part of the island, where the the elements might be so stable that they could be found in small amounts on earth [5]. By investigating the half-lives and decay energies of these elements, it will be possible to test models of the configuration of nucleons which governs these properties.

So far, the super-heavy elements at the very top of the chart of nuclides, as shown in figure 2, have been partially connected to each other. However, since all of them decay into isotopes that *fission* spontaneously, i.e. split into undetermined smaller fragments, before they reach known isotopes farther down the chart, their proton and neutron numbers are not unambiguously known.

One way to get an independent measurement of the proton number is to measure the radiation sent out in the form of X-rays during the decay of the atom. This is the purpose of an upcoming experiment, which sets out to verify at least one of the three of the isotopes of element 115 that have previously been claimed (marked with red in figure 2). The experiment is going to be performed

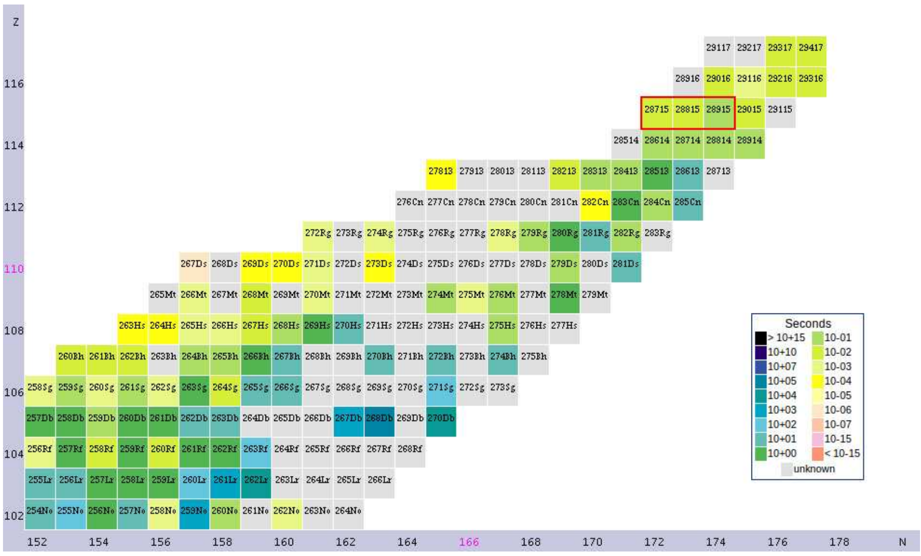

Figure 2: The heaviest elements synthesised so far. The isotopes that are to be synthesised and to be proven to represent element 115 in the upcoming experiment are indicated by a red square. Taken from Ref. [2].

at the GSI institute outside Darmstadt in Germany, where the Nuclear Structure Group from Lund University will play the key role within this international collaboration.

The Lund contribution consists of a detector set-up called TASISpec. This is specifically designed to allow for efficient detection of the X-rays that are emitted simultaneously with the alpha particles during the nuclear decay. TASISpec has been used previously and has been proven to work. In preparation for this experiment, however, some upgrades were made to the detector system. This thesis will cover the experimental set-up that will be used for the search for element 115, as well as the upgrades made to TASISpec. Additionally, the correction of a detector characteristic known as the dead layer that is used will be explained, including an attempt to optimize this procedure. Finally, a routine designed to turn off the accelerated particle beam when interesting events are registered will be covered.

2 Running a SHE Experiment with TASCA

There are two main constraints of a super-heavy element experiment. The first one is synthesis, as the atoms have to be created before they can be studied. However, as the produced nuclei grow heavier and heavier, the cross sections, and thus the production yields shrink rapidly. This makes the search for new elements increasingly difficult. For the very heavy elements that are searched for today, a single atom might be produced as infrequently as once per several months.

The second step is identification. Once the atom of a potentially new element is produced, it needs to be unambiguously identified. Here, one major issue is that the amount of undesired reaction products vastly outnumber the desired one, making it necessary to reliably separate these from each other. One device designed for this is TASCA (TransActinide Separator and Chemistry Apparatus), located at the GSI facility outside Darmstadt in Germany.

This section deals with the different parts involved in performing a super-heavy element experiment using TASCA. The general aspects will be covered, but where specifics are needed, the upcoming element 115 experiment will be used as an example. Thus, this section also serves as a description of the set-up that is going to be used for that experiment.

2.1 Synthesis

The steps involved in producing a new element will be covered here. First the type of nuclear reaction used to produce the SHE will be discussed, followed by the beam and target used to induce this reaction.

2.1.1 The Reaction

The super-heavy elements investigated at GSI are produced using heavy-ion-induced fusion-evaporation reactions, where heavy ions are colliding with a stationary target to produce SHE. The formation process can be divided into three stages [6]:

- First is the *capture* process, where the repulsive Coulomb barrier has to be overcome in order for the nuclei to touch each other. This requires the projectile to carry sufficient kinetic energy, described by Eq. (1):

  $$E_{kin} \geq \frac{1}{4\pi\epsilon_0}\frac{Z_1 Z_2 e^2}{R_t} - Q \tag{1}$$

  where ϵ_0 is the permittivity of vacuum, Z_1 and Z_2 the atomic numbers of the target and projectile nucleus, e the elementary charge, Q the Q-value of the reaction and R_t the distance between the centres of the two nuclei when thy touch each other. The Q-value is a concept in nuclear science representing the energy release in a nuclear reaction arising from the difference in binding energy of the reactants and products. SHE reactions are *endothermic*, meaning that the Q-value is negative, and the reaction requires a net input of energy to occur. An approximation of R_t can be obtained using the fact that $R \propto A^{1/3} = R_0 A^{1/3}$ where R_0 is roughly $1.2fm$ [7]. This gives

$$R_t \approx R_0 \left(A_1^{1/3} + A_2^{1/3} \right)$$

where A_1 and A_2 are the mass numbers of the two nuclei.

Another requirement relates to the need for a low *impact parameter*. The impact parameter is the distance between the centrers, perpendicular to the incoming trajectory of the projectile nucleus, i.e. the impact parameter is 0 for a head-on collision.

In the majority of cases the projectile is not captured, and so called quasi-elastic or deep-inelastic reactions result in the nuclei splitting up into target-like fragments (TLF) and projectile-like fragments (PLF). This process is illustrated in figure 3.

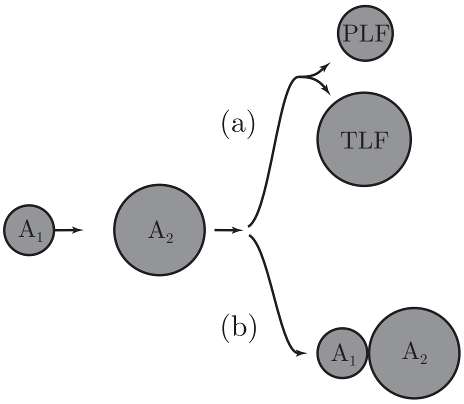

Figure 3: The first stage of the production of SHE. The nuclei can either form target-like fragments (TLF) and projectile-like fragments (PLF) and separate again, as in (a), or be captured, as in (b).

- After the system has undergone capture, the system can reconfigure its nucleons from this dinuclear system (DNS) into an almost spherical *compound nucleus*, and thus complete the fusion process. In order to do this it needs to traverse a saddle point of potential energy. For heavy systems, a more likely exit channel is for the DNS to split up in what is known as quasi-fission. This is illustrated in figure 4.
- Finally, the compound nucleus formed in (d) in figure 4 needs to reduce its excitation energy in some way. For the super-heavy nuclei considered in this thesis, the most likely way for it to do this is through regular fission. The more interesting alternative is to emit some of its neutrons, and subsequently γ-rays, in a process known as *evaporation* and statistical decay. The energy lost by emitting n neutrons and m photons can be written as

$$E_{lost} = \sum_n [S_i + T_i] + \sum_m E_{\gamma,i} \tag{2}$$

where S is the separation energy and T the kinetic energy of a neutron, and E_γ is the energy of a photon.

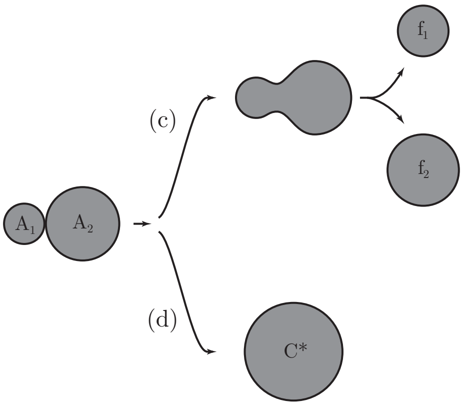

Figure 4: The evolution of the system after capture. The system can either undergo quasi-fission (c) or form a compound nucleus (d).

> The remaining desired nucleus is known as an *evaporation residue* or EVR for short. This step is illustrated in figure 5.

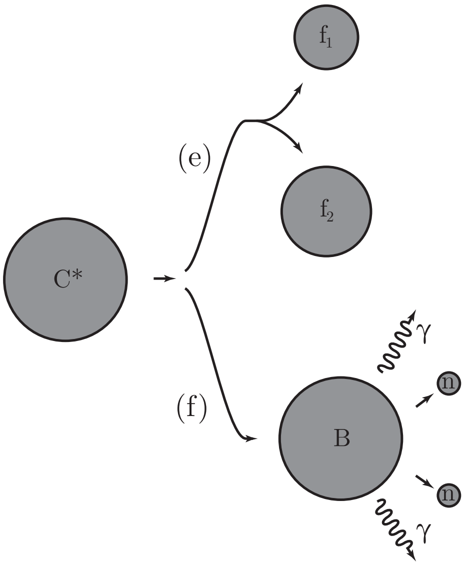

Figure 5: The de-excitation of the compound nucleus through either regular fission, as in (e), or through evaporation, as in (f).

The number of neutrons emitted in the last step is a function of the excitation energy of the compound nucleus, which is evident from Eq. (2), and which is related to the projectile energy. The exit channel is named after the number of neutrons that are evaporated. For instance, case (f) in figure 5 is an example of a $2n$ exit channel. This is used to search for specific isotopes, as the energy can be adjusted to maximize the cross section for the appropriate exit channel.

The probability of all these three steps (b -> d -> f) happening is very low, and the overall production cross section is thus very small, with the other branches of the reaction outweighing it by several orders of magnitude. The element 115 experiment will use ^{243}Am as target with a ^{48}Ca beam. The goal is to produce element 115 through the 2-4n channels. The cross sections are on the order of picobarn ($1 \cdot 10^{-12} b = 1pb$), as can be seen in figure 6.

Barn is a unit of cross section corresponding to $10^{-28} m^2$ or $10^{-24} cm^2$, meaning that a picobarn is $10^{-36} cm^2$. The etymology behind it is rather odd, and dates back to the development of the atomic bomb in the 1940s, when the American physicists described the uranium nucleus, being the heaviest naturally occurring element, as "big as a barn". They used this unit, roughly corresponding to the cross sectional area of a uranium nucleus, to obfuscate the nature of their research, probably not expecting it to become the standard unit of cross section in nuclear and particle physics that it is today.

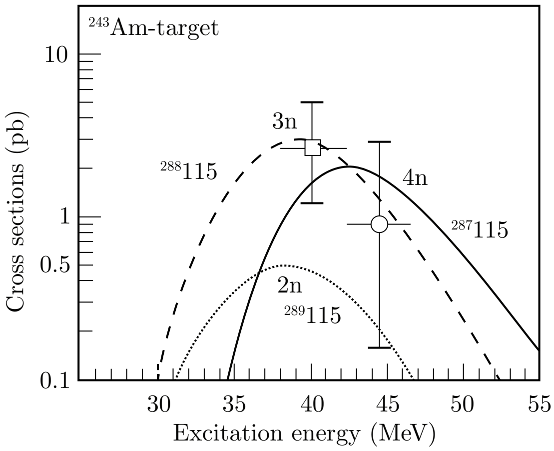

Figure 6: The cross section for the 2-4n channels in the reaction ^{243}Am(^{48}Ca,2-4n)$^{287-289}$115. Taken from [8].

Beam intensities are typically of the order of 1 particle μA ($p\mu A$), which is a unit commonly used in physics involving ions. The same particle rate, i.e. the number of ions per second, will correspond to different electrical currents (μA) depending on the charge state of the ions. The unit particle μA scales the ion charge to unity to allow for easier comparisons of the intensities between beams of ions with different charge states, and consequently, $1 p\mu A = 6.25 \cdot 10^{12}$ particles per second.

To get a sense of the resulting yield, the rate of a typical target of thickness $0.7 mg/cm^2$ being irradiated by $1 p\mu A$ to produce a reaction with a cross section of 1 pb is calculated below using the rate equation [Eq. (3)].

$$R = \Phi \sigma \rho \tag{3}$$

where Φ is the incoming beam flux per area, σ is the macroscopic cross section and ρ is the density of atoms. Using the typical values above, we get

$$
\begin{aligned}
R &= 1\mu A \cdot 1pb \cdot 0.7mg/cm^2 \\
R &= \frac{1 \cdot 10^{-6}A}{1.6 \cdot 10^{-19}As} \cdot 1 \cdot 10^{-12}b \cdot 10^{-24}cm^2/b \cdot \frac{0.7 \cdot 10^{-3}g/cm^2}{243g/mol} \cdot 6 \cdot 10^{23}/mol \\
R &\approx 1.08 \cdot 10^{-5}/s \\
R &\approx 6.53/\text{week}
\end{aligned}
$$

This rough estimation shows that the production rate is of the order of one atom per day, before factors such as transmission through the separator or detection efficiency has been taken into account.

2.1.2 The Beam

Once the appropriate reaction channel has been decided upon, the projectile nucleus has to be accelerated to an energy which gives the highest possible cross section for this reaction to occur. At GSI, this is performed by the *Universal Linear Accelerator*, or UNILAC for short.

The UNILAC is a pulsed accelerator, producing beam bunches, called macropulses at a frequency of 50 Hz. Each macropulse consists of many consecutive micropulses, which are only a few nanoseconds in duration. The beam structure is illustrated in figure 7, and is a result of the radio frequency quadrupole (RFQ) used by the UNILAC.

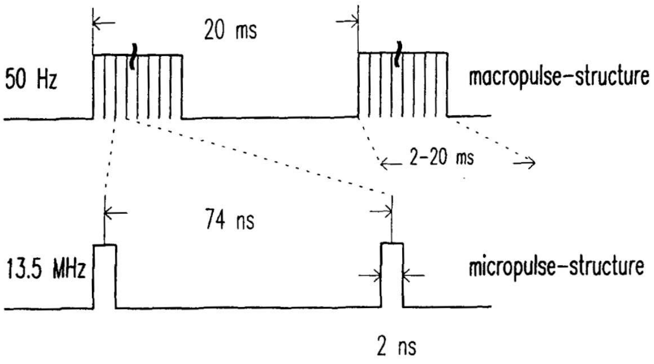

Figure 7: The beam structure of the UNILAC. Image from N. Angert [9].

The accelerator consists of many parts, but in short, the first major part is an ion source, of which there are a few different types to choose from at GSI, depending on the ion and/or energy that is needed. A gas stripper is used to strip electrons from the nuclei, after which the desired charge state for consecutive acceleration can be chosen. The acceleration is performed by radio frequency cavities. Afterwards, the ions are sent to different branches, or "caves", depending on which experiment is using the beam. A schematic view of the UNILAC can be seen in figure 8.

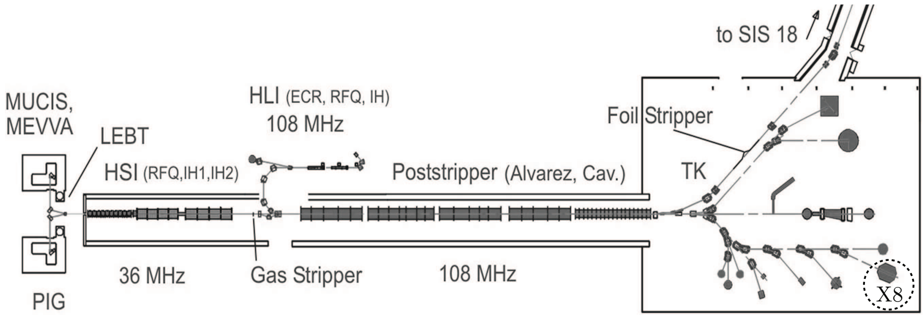

Figure 8: An overview of the UNILAC. TASCA is located in X8 (the eighth cave of the X-branch at the bottom right). Image from the GSI website [10].

2.1.3 The Target

The ions that have been accelerated need to be able to react with the target nuclei under controlled circumstances. For the heavy and radioactive actinide targets used in SHE research, this is typically done by depositing the target material on a suitable backing material using electrolysis. A material with a low atomic number, such as C, Al or Ti, is often used to avoid producing elements whose decay might interfere with the detection of the desired reaction product. In addition, the chosen material needs to be resilient to the high temperatures that are occurring when the target is irradiated.

The target should be sufficiently thin to minimize the energy loss the particles experience as they pass through the material, and as a result, foils only a few micrometers thick are used. As titanium shows superior mechanical integrity compared to aluminium and carbon [11], it is most often chosen. This is also the case for the americium target that is to be used in the element 115 experiment.

Due to the high intensity of the particle beam, the target cannot be stationary, as it would simply melt. To circumvent this, the target segments are arc-shaped and placed together to form a wheel. This wheel rotates synchronously with the frequency of the UNILAC, so that the beam irradiates one segment at a time for each macropulse. The target wheels that are currently used by TASCA consist of four such segments (see figure 9).

2.2 Identification

At this point the nucleus is produced (albeit at a very low rate), and the following sections will cover the steps involved in identifying the evaporation residue (EVR).

2.2.1 The Separator - TASCA

While the target is being irradiated, a wide variety of particles emerge on the other side. This can be beam particles that have passed through the target without reacting, target nuclei that have been knocked out from the target, projectile-like and target-like fragments (cf. figure 3), fission fragments as a result of quasi-fission (cf. figure 4) and in very, very rare cases, fusion-evaporation

Figure 9: One of the TASCA target wheels. The diameter of the wheel is 100 mm.

products (figure 5). The purpose of the separator is, as the name suggests, to separate these rare events from the legions of unwanted particles.

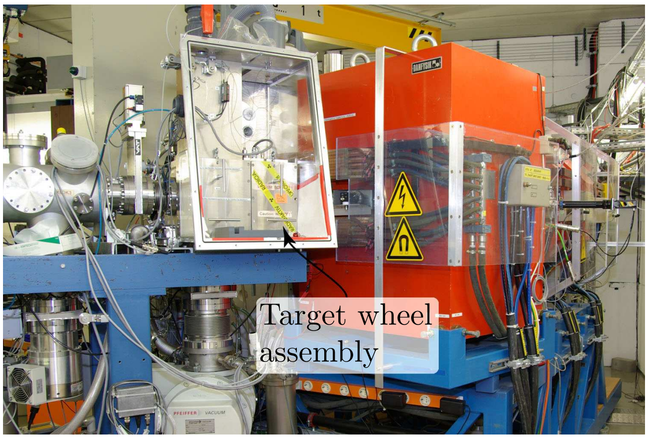

Figure 10: The target wheel assembly of TASCA. The beam enters from the left side of the picture.

Most separators take advantage of the fact that ions are charged, and thus can be accelerated by the Lorentz force using either an electrostatic or static magnetic field. The design that is chosen depends on experimental factors, such as how large the differences in mass and charge between the particles are, what transmission is needed, etc.

In the case of EVRs, as high transmission as possible is desirable due to the small cross sections. The reaction products also have some variations in velocity and recoil vector, and a wide distribution of charge states, typically on the order of 10-15 charge states [12]. These result in different trajectories through the separator. This difficulty can be overcome by filling the separator with a dilute gas; usually helium at a pressure of about 1 mbar. This causes the particles to undergo charge altering collisions on their way through the separator, and after a statistically significant number of such collisions, the charge state of the particles will converge around an average charge state, q_{av}. However, the presence gas implies that an electric field of the strength needed for the purpose of deflections cannot be maintained without discharges. Consequently, gas-filled separators rely solely on magnetic fields for separating ions.

The average charge state depends on the velocity and proton number of the ion [12]:

$$q_{av} = \frac{vZ^{\alpha}}{v_0} \tag{4}$$

where v is the velocity and Z the proton number of the ion, v_0 is the Bohr velocity, and $\alpha = 1/3$. This can be combined with the following kinematic expression:

$$B\rho = \frac{mv}{qe} \tag{5}$$

where B is the magnetic field, ρ the curavture of the trajectory, m the mass, v the velocity and q the charge of the ion and e is the elementary charge. If we assume that the ion charge is the average charge state from (4), we get:

$$B\rho = \frac{mv}{\frac{vZ^{\alpha}}{v_0}e} \approx 0.0227\frac{A}{Z^{\alpha}} \tag{6}$$

where the numerical values of the physical constants have been used. The important point to note here is that $B\rho$, i.e. the curvature of the trajectory for a given magnetic field, often called the *magnetic rigidity*, is independent of the initial velocity and charge state of the ion. Gas separators thus have a wide acceptance with regard to these two properties, making them well suited for experiments with EVRs. This relies on the fact that $\frac{A}{Z^{\alpha}}$ of the EVRs differ enough from the target-like and projectile-like particles to allow for a good separation. For more in depth coverage of charge states and charge changing collisions, refer to Ref. [13].

TASCA, the gas-filled separator that is focused upon in this section, consists of three successive magnets [14]. The first one after the target is a dipole, which performs the main separation as particles with different magnetic rigidities will have different curvatures to their trajectories. Based on Eq. (6), a suitable strength of the magnetic field can be determined. The two subsequent magnets are quadrupoles. Their purpose is to focus the EVRs on their way to the focal plane, one focusing in the horizontal and the other in the vertical direction. A schematic overview of TASCA can be seen in figure 11(a).

TASCA can be used in two modes, depending on the order of the focusing magnets. If the first quadrupole is set to focus horizontally and the second vertically, commonly known as a DQ_HQ_V configuration, the separator runs in what is called *high transmission mode*, or HTM for short. This results in a high transmission on the order of 50-60 %, at the cost of a relatively spread out image at the focal plane. If the order of the focusing is reversed, the resulting DQ_VQ_H configuration is called *small image mode* or SIM. As the name suggests,

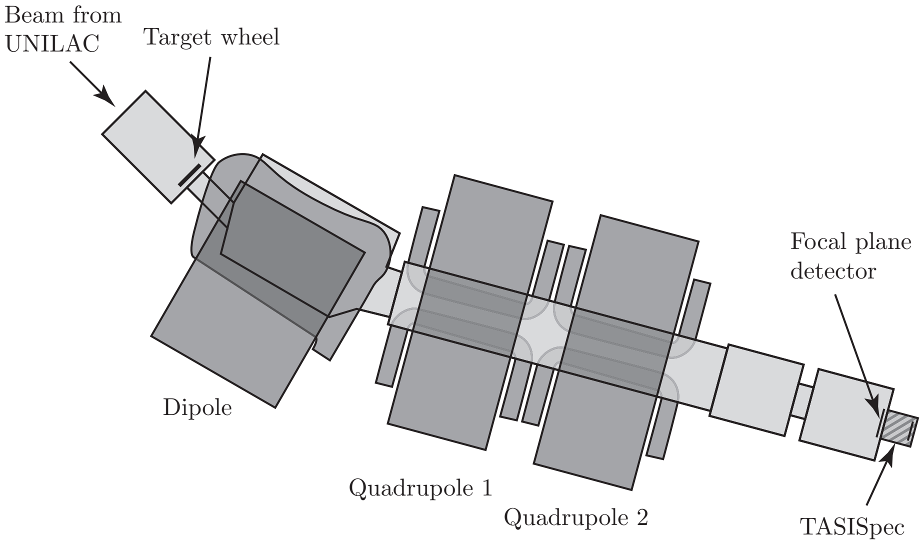

(a) A schematic overview of the TASCA separator. TASISpec is depicted at the end of the separator. Note that either the focal plane detector *or* TASISpec is used; they cannot be used at the same time.

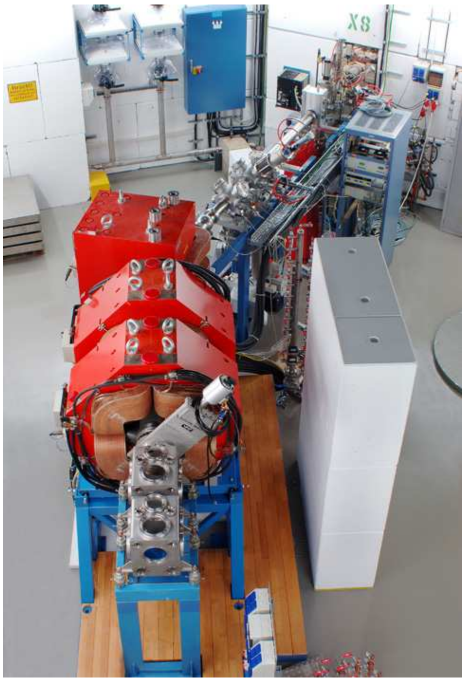

(b) A photo of TASCA during installation. The beam enters the cave through the wall at the spot marked "X8". The three red pieces close to the camera are the magnets. Image from TASCA website [15].

Figure 11: The TASCA separator.

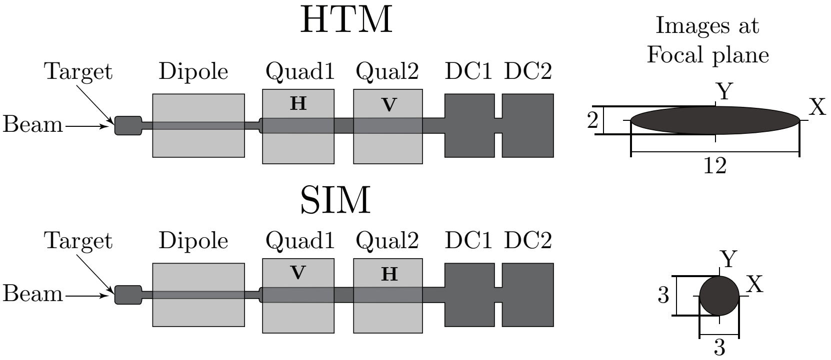

Figure 12: An overview of the two modes of TASCA. The top one shows HTM, which allows for a greater transmission at the cost of a larger image at the focal plane compared to the SIM depicted at the bottom. DC1 and DC2 are the two detector chambers at the end of the separator. Measurements are in cm. Image taken from [16].

this mode has a much smaller image at the focal plane, but has a slightly lower transmission of 30-40 % [16]. An overview of the two modes is given in figure 12.

2.2.2 The Detectors

Once the EVRs have made it through the separator they need to be detected using one or more detectors placed at the focal plane [see figure 11(a)]. The set-up used together with TASCA varies with the experimental circumstances, so this section will use the planned element 115-experiment as an example of what such a set-up typically looks like.

The produced element is identified through its decay chain. The different element 115 isotopes all decay through a series of α-decays followed by spontaneous fission. The decay chains are shown in figure 13. Correct α-energies thus have to be registered, followed by the high-energy signal produced by a fission event.

Most experiments at TASCA uses the *focal plane detector* at the end of the separator as the main detector. This is a double-sided silicon strip detector (DSSSD) into which the EVR is implanted. The DSSSD is a semiconductor detector where the readout is performed through aluminium strips running perpendicular with respect to each other on the front- and backside. This provides both spatial information and the energy of the charged implanted or decay particle.

However, in the mentioned element 115-experiment, the standard TASCA focal plane detector will not be used. Instead a detector system called *TASISpec* [17] (**TA**SCA **S**mall **I**mage mode **Spec**troscopy) will be positioned at the end of TASCA and will act in the same way as the focal plane detector [see figure 11(a)]. TASISpec also consists of an *implantation detector* in the form of a DSSSD with 32 strips on either side, which is surrounded by four DSSSDs called *box detectors* with 32 strips vertically and horizontally, which are connected in pairs to reduce the amount of electronics channels. In total, five sides of a cube are covered, as shown schematically in figure 14. The purpose of the box detectors is to increase

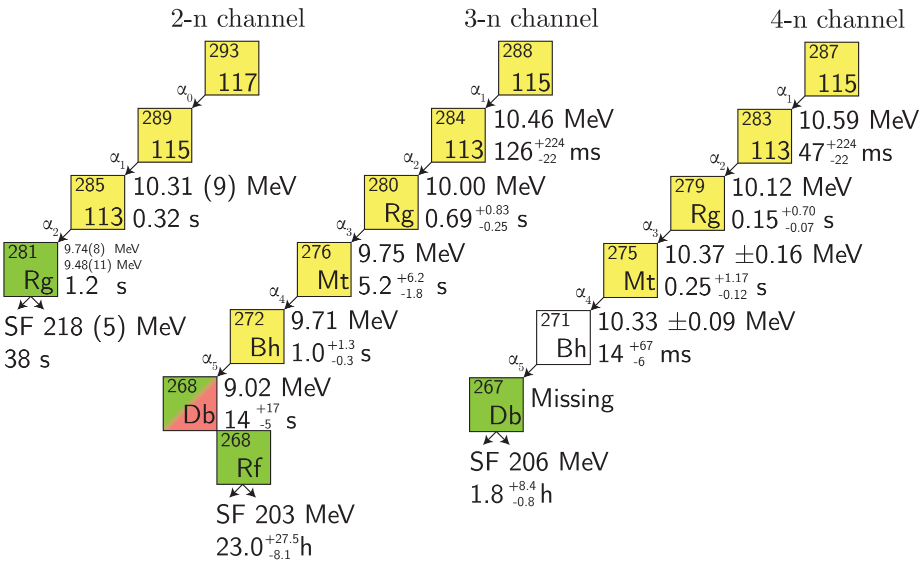

Figure 13: Decay chains proposed for the $2n$-, $3n$- and $4n$- channels for element 115. Alpha-decay energies and half-lives are taken from Refs. [3] and [8].

the α-detection efficiency as the α-particles only have a 50 % chance of being emitted into and hence detected by the implantation detector. As a result, the α-efficiency is roughly 80 % [17].

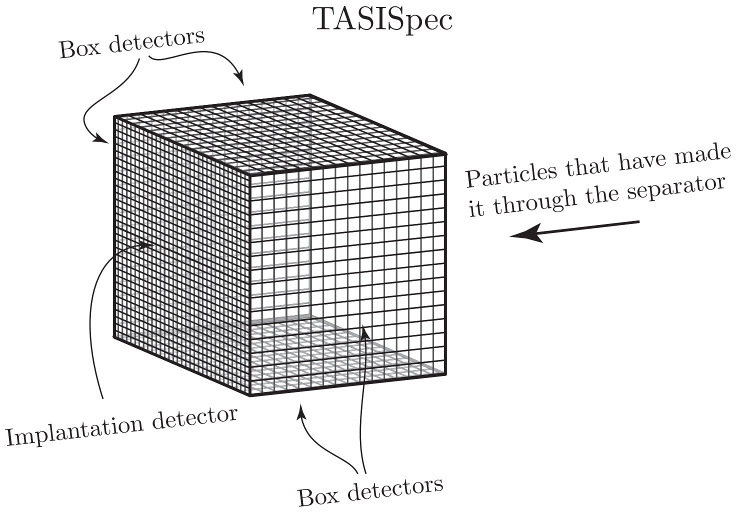

Figure 14: A schematic overview of the TASISpec silicon detectors.

These silicon detectors are encased in a relatively thin aluminium chamber [0.5-1.0 mm, in comparison with the roughly 1 cm thick stainless steel walls of the detector chamber seen in the foreground of figure 11(b)]. This allows even low energy γ-rays ($E_\gamma \gtrsim 30$ keV) to pass through with relative ease, which is the main strength of TASISpec. Due to its protruding position at the end of the

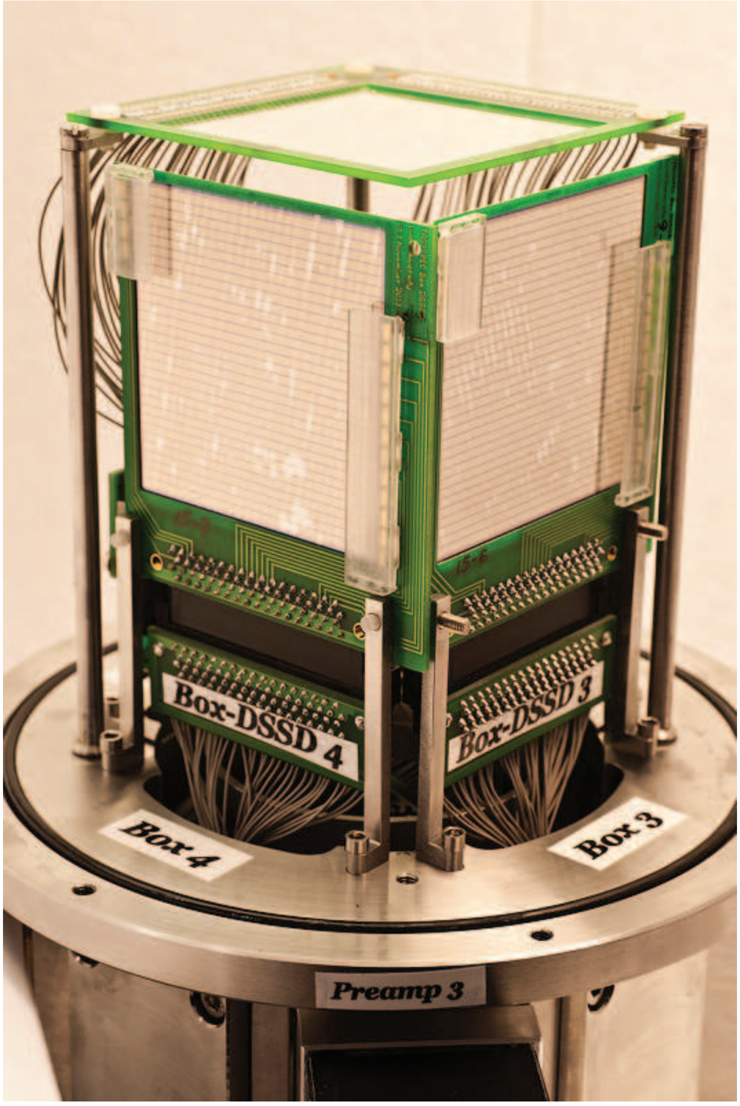

Figure 15: A photo of the TASISpec silicon detectors. The set-up mounts to TASCA at the bottom of the image.

separator and its thin chamber, γ detectors can be placed behind each wall of the chamber, allowing for high γ-detection efficiencies. Usually a germanium-clover is placed behind each box detector. This is a germanium detector consisting of four more or less rectangular crystals, which provides some spatial information. Behind the the implantation detector, a germanium-cluster, consisting of seven hexagonal crystals, is used [17].

Since the detection efficiencies for both α-particles and γ-rays are high, coincidence spectroscopy between the two becomes possible. The characteristic X-rays emitted by an element is determined by the atomic number of the nucleus through what is known as Moseley's law, which states that the frequency

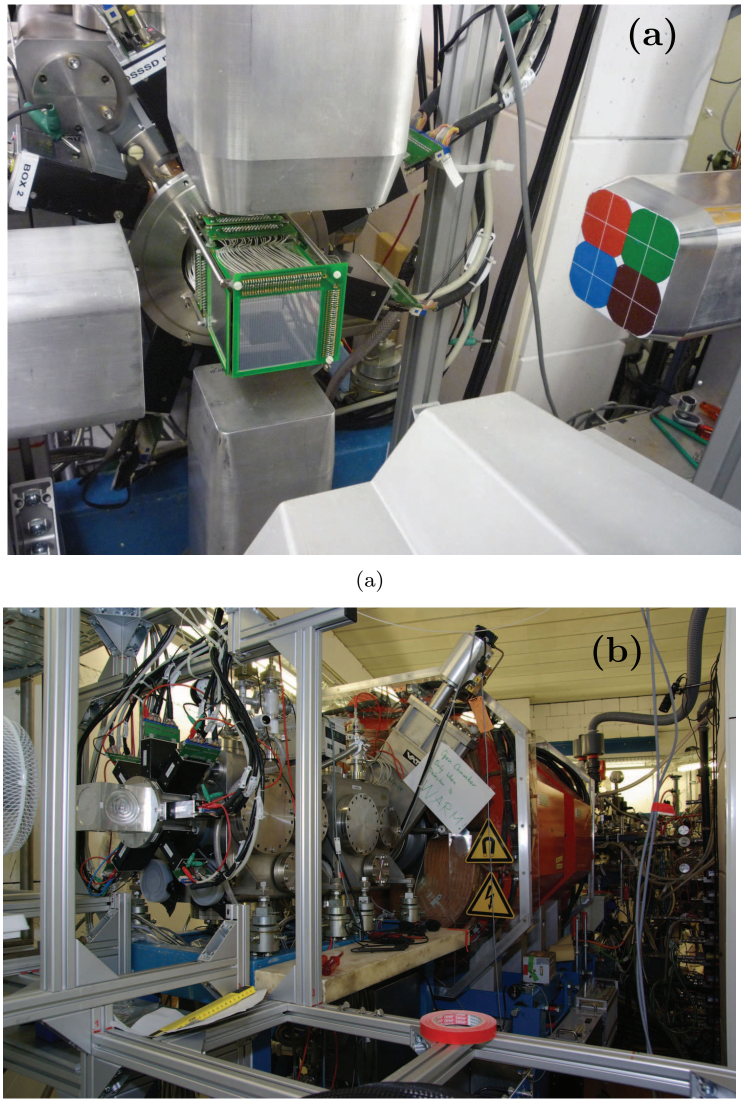

(a)

(b)

Figure 16: (a) A photo of TASISpec without the chamber, making the silicon detectors visible. The five germanium detectors are seen around the five sides. (b) TASISpec with the chamber, mounted at the end of TASCA.

of the K X-rays, $f_k = 2.48 \times 10^{15}(Z-1)^2$ Hz. This means that if X-rays emitted coincidentally with the α-decay can be detected, they serve as a fingerprint for the proton number of the daughter, and hence also mother, nucleus.

2.2.3 Electronics

Just like the combinations of detectors used, the electronics can vary significantly between experiments. The core functionality, however, is always to convert the analogue signals from the detectors to digital ones that can be recorded and analysed. This is done using analogue-to-digital converters (ADCs) which map the input signal to a series of bits. The number of bits depends on the resolution of the ADC.

In addition to the amplitudes of the signals, the time between events is also recorded using a multihit TDC (time-to-digital converter). Other than that, the set-up might also record, for instance, the state of the beam, i.e. whether there is a macro pulse or not at any given time, which target segment is used, or indication of possible sources of noise, such as the automated filling of liquid nitrogen for the germanium detectors. Like in the previous section, the element 115 experiment will be used to give an example of what components might be utilized.

Each of the strips of the implantation detector is connected to a *preamplifier* which amplifies the signal from the detector to a typical range of 1V/20 MeV down to 1V/200 MeV radiation energy. Since this stage is most sensitive to noise, the preamplifiers are placed as close to the detector as possible to minimize the cable length. Traditionally, the amplified signal is then sent to a *shaping amplifier*, which shapes the pulse and amplifies it further. The shaping is done to allow the pulse to return to its baseline more quickly, thereby enabling the system to handle higher count rates. If sampling ADCs, i.e. ADCs which samples and records the pulse shape, thereby allowing for pulse shape analysis, are used, they are connected directly to the preamplifier, as the shaper will obviously distort the pulse shape. The use of TASISpec together with sampling ADCs is described in Refs. [18] and [19].

Each channel from the preamplifier is sent to two shaping amplifiers with different gains. The purpose of this is to have a good energy resolution both in the range of α-decay and fission events. Thus, one of the shaping amplifiers is set to have an output range of 0-15 MeV, called *high gain*, and one in the 0-220 MeV range, called *low gain*. These shaped and amplified signals are finally sent to the ADCs, where they are converted and read out by the data acquisition system.

The signals from the box detectors undergo basically the same treatment, with one exception. Instead of single shaper channels used for each strip of the implantation detector, multiplexing shapers are used. These take eight channels as input and output only the shaped signal with high and low gain of the signal with the highest amplitude for a given event. In addition to this it also outputs a bit pattern corresponding to the identity of the channel which was sent to the output. This means that the amount of ADCs can be reduced by a factor of eight, and only one ADC module is needed for the box detectors instead of eight.

However, while the multiplexing reduces the amount of ADCs, it calls for the need of *latches*. These modules take the three bits from each multiplexed shaper and collect them to a single bit pattern in the data stream, which allows for deconvolution of the data during the analysis. An overview of this set-up can be seen in figure 17.

The germanium detectors consist of a self-contained package of crystals and preamplifiers, and the signals are sent directly to the above-mentioned sampling ADCs.

A *pattern unit* is used to record the state of the set-up in the data stream. This module has a series of binary inputs and outputs which can be connected

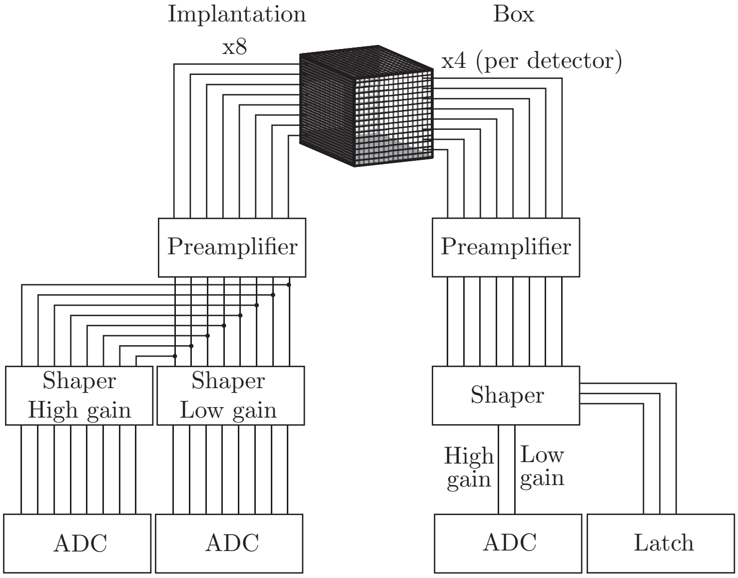

Figure 17: An overview of the electronics of the TASISpec element 115 experiment. Since the implantation detector has 64 strips in total, there are eight groups identical to the one on the left of the figure in parallel. Similarly, each box detector has 2x16 strips, making four groups like the one on the right per detector, resulting in 16 groups for all four of the box detectors.

to various signals. In this case two of the inputs are used to indicate which of the target segments is currently being irradiated (two bits equal four combinations), one to indicate beam-on, i.e. a signal which is high during a macro pulse, another which is the same signal delayed 0.2ms and a third which is a logical OR of the two beam signals to form a beam-on signal which is sure to cover the entire macro pulse.

The beam signals can be used in the analysis to select events that are in beam-off periods, as the background is significantly higher during beam-on periods. Furthermore, the automated filling of liquid nitrogen of the germanium detectors might also introduce anomalies in the data stream, and a signal indicating that filling is ongoing will be connected to the pattern unit in the future.

In addition to the modules mentioned, there are a number of mainly logic units, which are used to, for instance, split signals, generate gates, convert signals between different standards (NIM, TTL, etc.), delay signals, etc. While essential for a functional set-up, they are not necessary to understand the basic functionality of the electronics and what information is recorded during the experiment. Thus, they are omitted from this section. The entire electronics set-up can be seen in figure 18.

2.2.4 Data Collection

The final part needed to run an experiment is to record the data that is being put out by the modules mentioned above. At GSI this is done using a data acquisition framework called MBS (short for Multi Branch System) [20]. As the

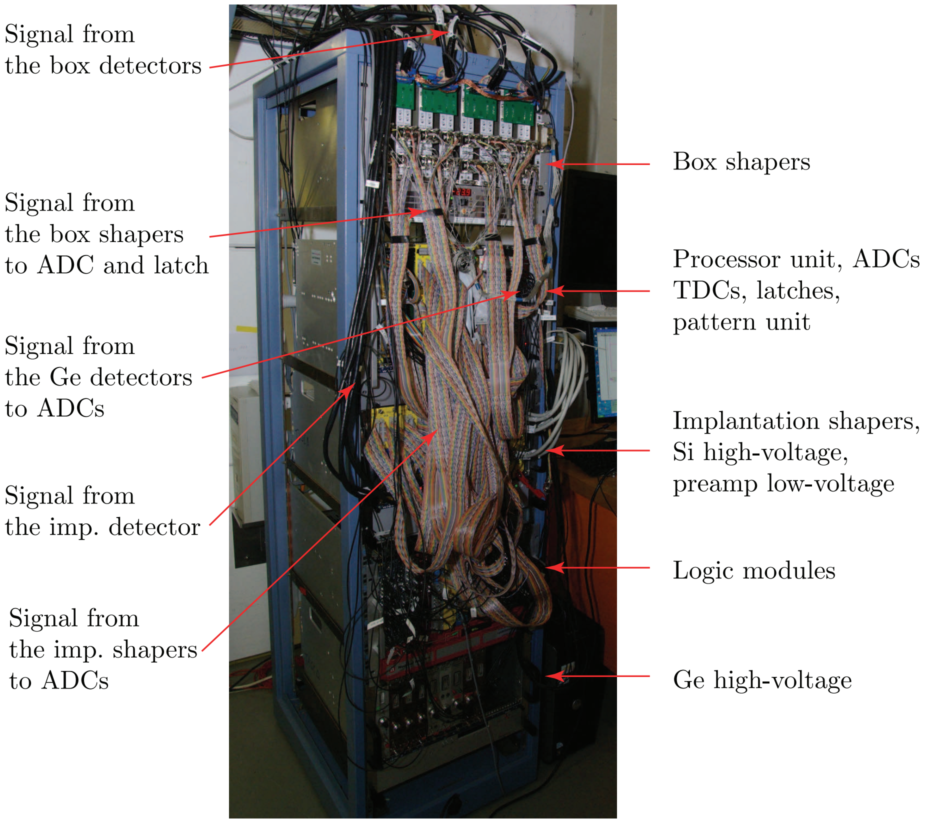

Figure 18: A photography of the electronics that is to be used during the element 115 experiment. Detector signals and crate modules are labled. 192+23 high-resolution channels and trigger and DAQ logics are collected in one rack.

name suggests, this allows for several crates (like the central one seen in figure 18) to be connected together to form a single data stream. Each branch has a processor unit running the software, as well as (at least) one trigger module. The master trigger module will handle the triggers originating from different modules and create an accepted trigger. This sends a message to the processor unit, informing it that an event is ready for readout. Another accepted trigger is prevented until the readout is complete. For the 115 experiment, an accepted trigger signal is sent to the input of the pattern unit to allow for an additional sanity check of the data acquisition system.

Readout routines pass the data from the modules via memory segments known as subevent pipes to a task running on the CPU called the collector. The collector combines the subevents into one complete event which is placed in a buffer. This buffer can then be sent to either online analysis and/or to offline storage in the form of disk or tape.

The MBS is described in more detail in Refs. [20] and [21].

3 Element 115 Preparations in Lund

A VITAL PART of the element 115 experiment is obviously the TASISpec set-up. It was used to search for K-isomers of ^{253}No during 2010, meaning that the set-up has been utilized and tested. In preparation for the element 115 experiment, however, a few modifications and upgrades were made. The first was to exchange the box detectors from single-sided to double-sided silicon strip detectors, and the second to use new ADCs for the silicon detectors.

3.1 TASISpec DSSSD Box Detectors

Early on in the preparation of the element 115 experiment, the box detectors of TASISpec were upgraded. Originally, the detector system consisted of a DSSSD implantation detector surrounded by four single-sided silicon strip detectors (SSSSD) with the strips running along the beam direction. The SSSSDs were exchanged for DSSSDs in order to improve the spatial resolution of the box detectors. This allows for software compensation for the *dead layer* of the detector, which, due to the geometry of the set-up, decreases the energy resolution significantly. This effect, and the compensation, will be covered in greater detail in a later section. The increased number of electronics channels resulting from this upgrade, meant that some recabling had to be done.

3.1.1 Feedthroughs and Cabling

The cabling of the implantation detector is realatively straightforward as it consists of 2x32 channels. Each of the preamplifiers takes 32 channels, meaning that the cabling consists of connecting channel 1-32 of the p-side to the channels 1-32 of the first preamplifier, and channel 1-32 of the n-side to the corresponding channels of the second preamplifier. In the case of the box detectors, however, the cabling is a bit more complex for two reasons.

Firstly, due to spatial reasons, i.e. leaving as little dead space as possible around the detector, the pins of the connector mounted in the detector PCB do not correspond to the consecutive channels of the detectors. An overview of which strips are connected to which connector pin can be seen in figures 19 and 20. This is disentangled by the cables running from the connector on the detector PCB to the preamplifier connector on the outside of the chamber so that the preamplifier receives the channels in consecutive order.

Secondly, each box consists of 2x16 channels. Since the preamplifier has the same polarity for all 32 channels, the detectors must share the preamplifiers so that one preamplifier is responsible for the p-sides of two detectors, and another for the n-sides of two detectors. The relations between the detectors and preamplifiers can be seen in table 1. For example, pin 0-15 of preamp 1 corresponds to strip 0-15 of the p-side of box 1 and pin 16-31 corresponds to strip 0-15 of the p-side of box 2.

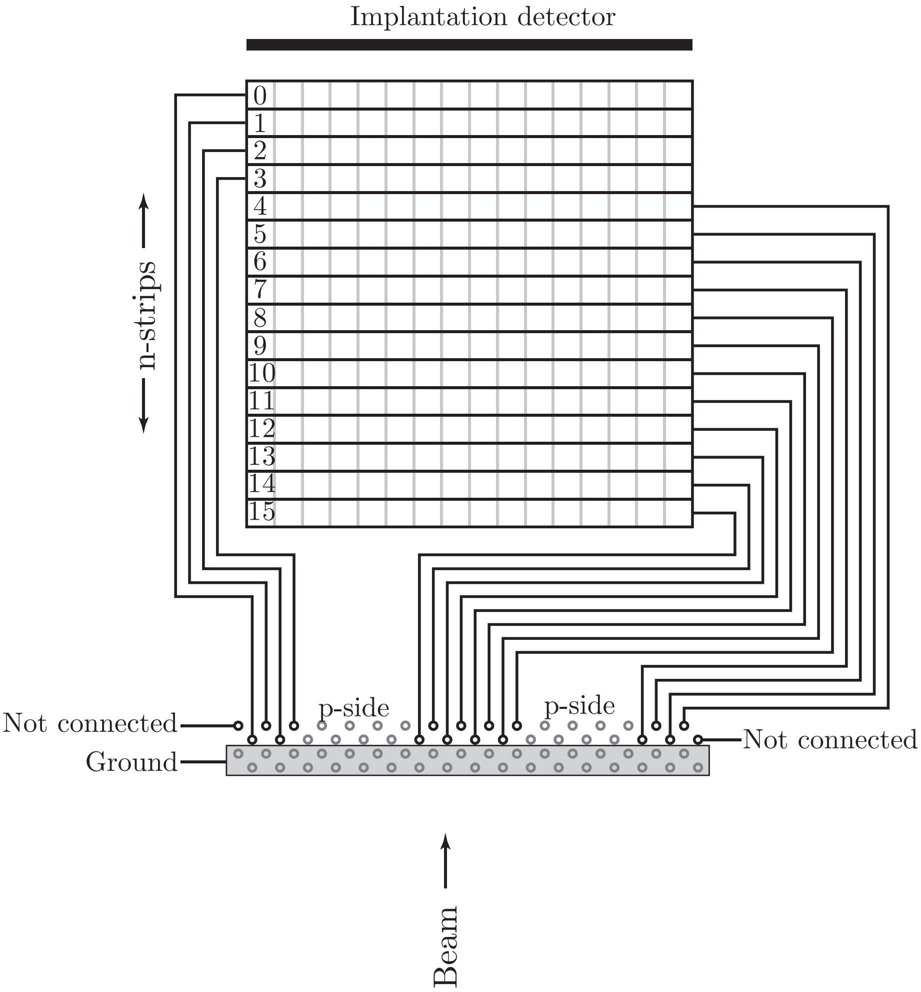

Figure 19: The connections from the n-side strips to the box connector seen from the outside of TASISpec.

Table 1: The connection between the detectors and the preamplifiers.

Preamp	Detector	Side
1	Box 1+2	p-side
2	Box 1+2	n-side
3	Box 3+4	p-side
4	Box 3+4	n-side
5	Implantation	p-side
6	Implantation	n-side

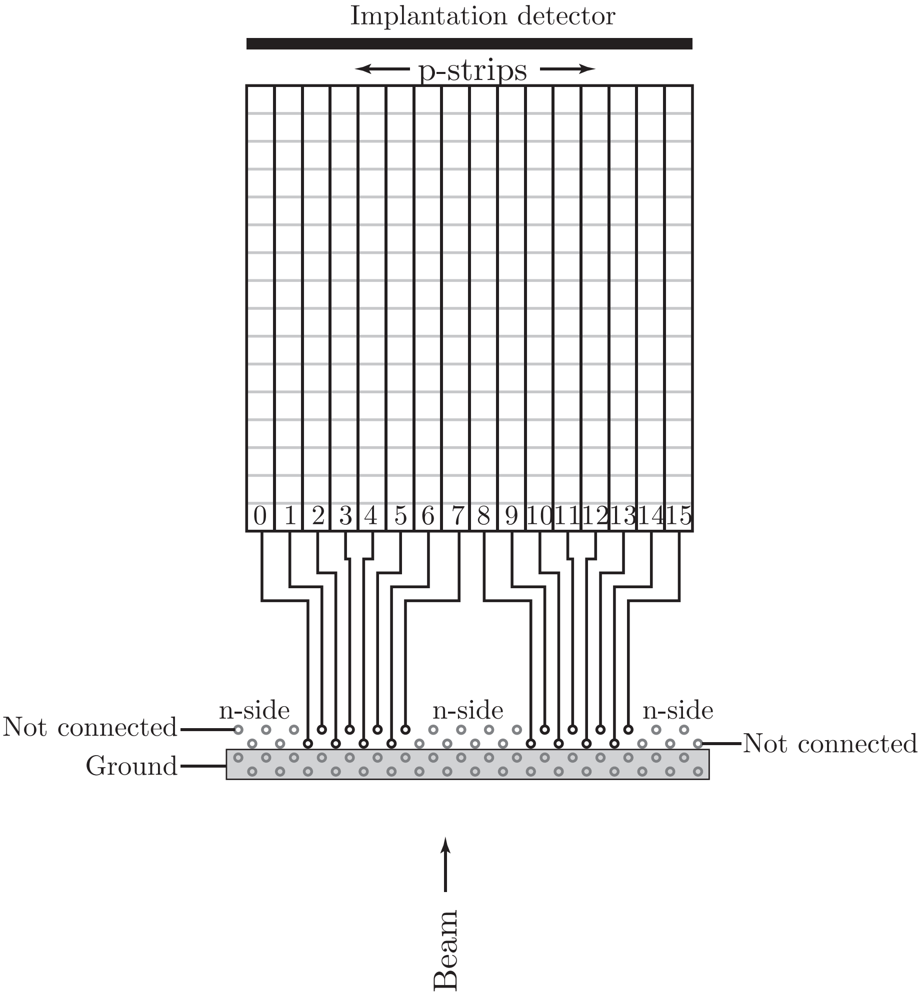

Figure 20: The connections from the p-side strips to the box connector seen from the outside of TASISpec. Note that the p-strips run on the inside of TASISpec, i.e. the picture sees through the PCB to offer the same point of view for the connector as in figure 19.

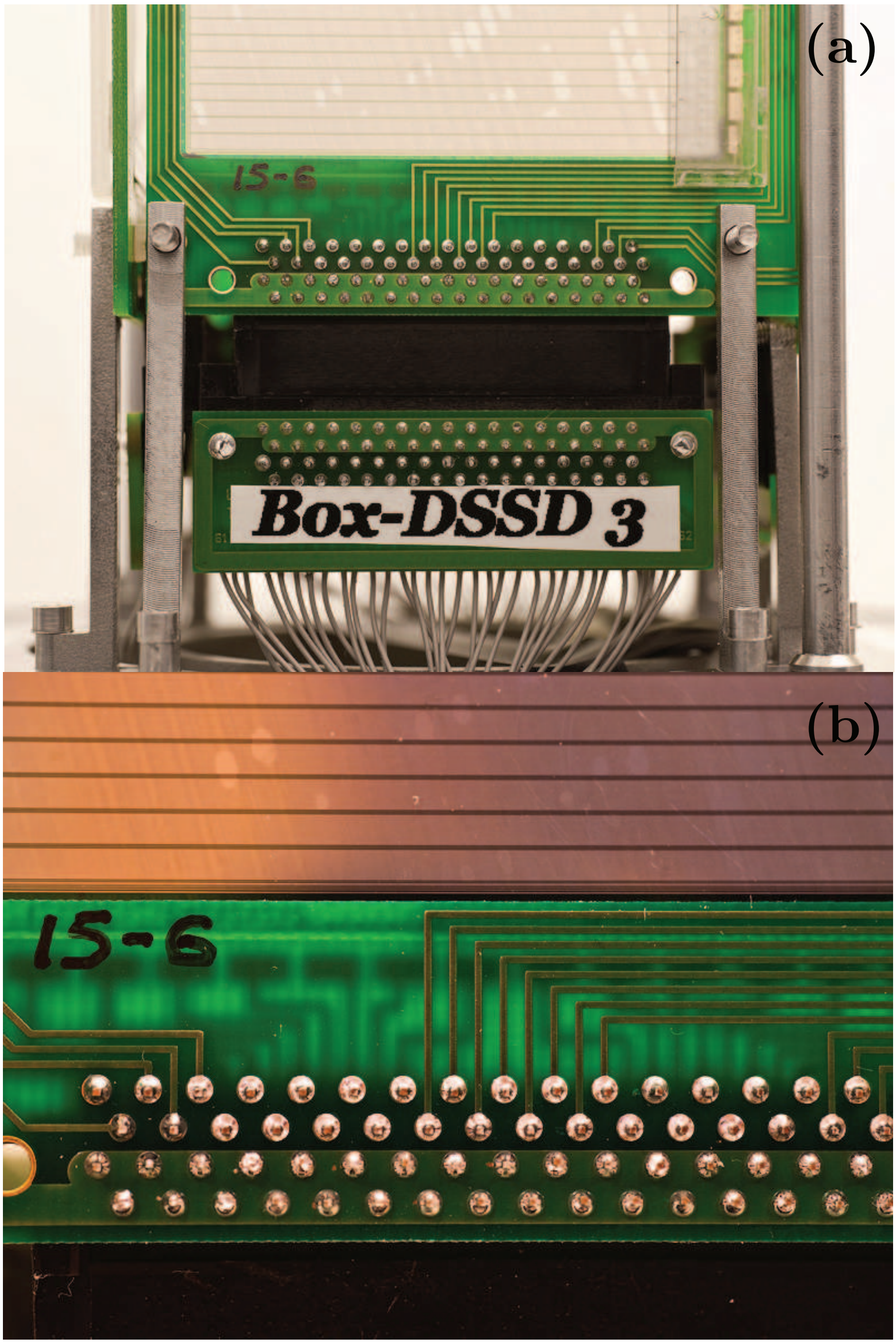

Figure 21: Two close-ups of a TASISpec box detector where the n-strip traces are visible on the PCB. The p-side traces can be hinted, running on the other side of the PCB.

3.1.2 Check of Cabling and Electronics

In order to make sure that all the strips end up at the right position in the data stream, a simple test was performed. This consisted of putting shields of different shapes made from paper and wire in front of an ^{241}Am alpha source placed inside TASISpec. The set-up is shown in figure 22. By looking at the resulting *hit pattern*, it is possible to deduce if the cables are correct by looking for the patterns corresponding to the shields. The hit pattern is simply a graph showing the number of hits of each pixel. The pixel signal is created by looking for coincident signals in the p- and n-strips of a detector.

The resulting hit patterns (figure 23) are consistent with the expected patterns from the test setup. Thus, the cabling is correct and all detector and electronics channels are functioning.

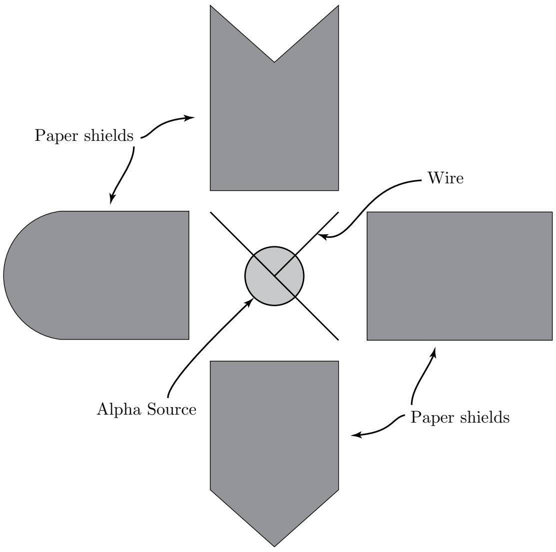

Figure 22: The setup of the shields folded out as seen from the implantation detector of TASISpec.

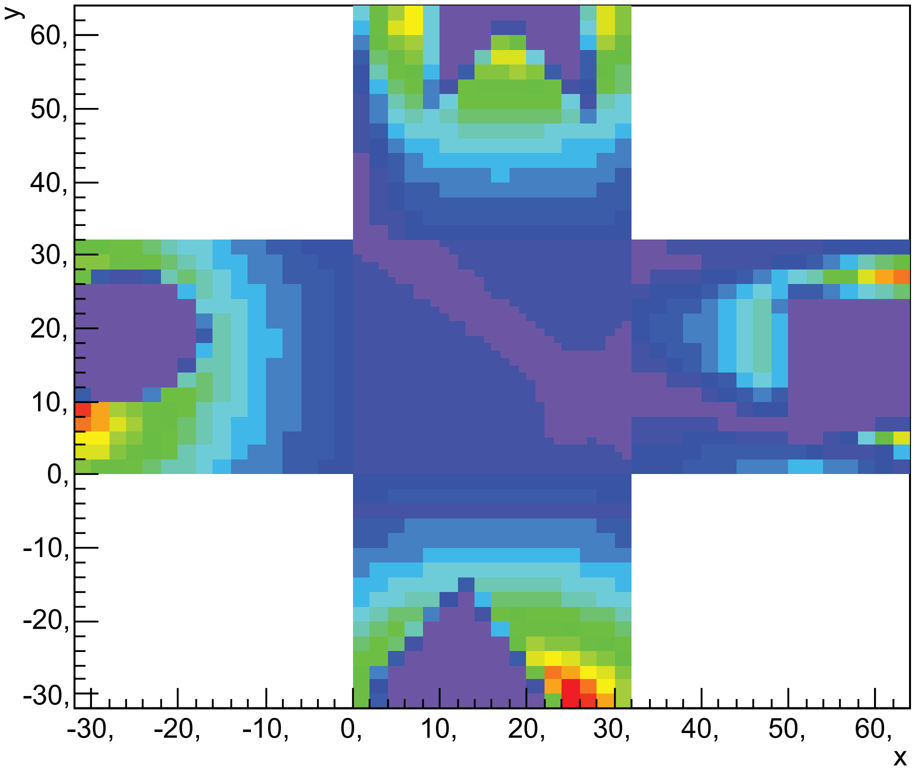

Figure 23: The implantation hit pattern for the cabling test.

3.1.3 Dead Layer Correction

Exchanging the SSSSDs of the box detectors with DSSSDs allows for a better spatial resolution of the particles emerging from the implantation detector. This makes it possible to achieve a better energy resolution due to the ability to compensate for a feature known as *dead layer* present in all silicon detectors.

The dead layer is simply an insensitive layer of silicon outside the sensitive detector volume, with a thickness of the order of $\sim 1\mu\text{m}$. This means that the incoming particles will lose some of their energy as they pass through this layer before their energy loss is registered by the sensitive volume of the detector. This poses no big problem for the implantation detector as the alpha particles originate from the EVRs. These nuclei have been implanted several microns deep due to the momentum which allowed them to pass through the separator, which positions them inside the sensitive volume.

However, this is not true for the particles reaching the box detectors. Since these originate from the implantation detector, they will have to pass through two dead layers before they can be detected. To further complicate things, the distribution of their incident angle will vary from close to perpendicular for the particles hitting the edge of the box detector closest to the implantation detector to close to 25 degrees for the ones hitting the furthermost edge. The effective dead layer experienced by the particle will thus be more than twice as thick for these particles, meaning that the undetected energy loss will have a spread depending on the trajectory of the particles, which is demonstrated by figure 24.

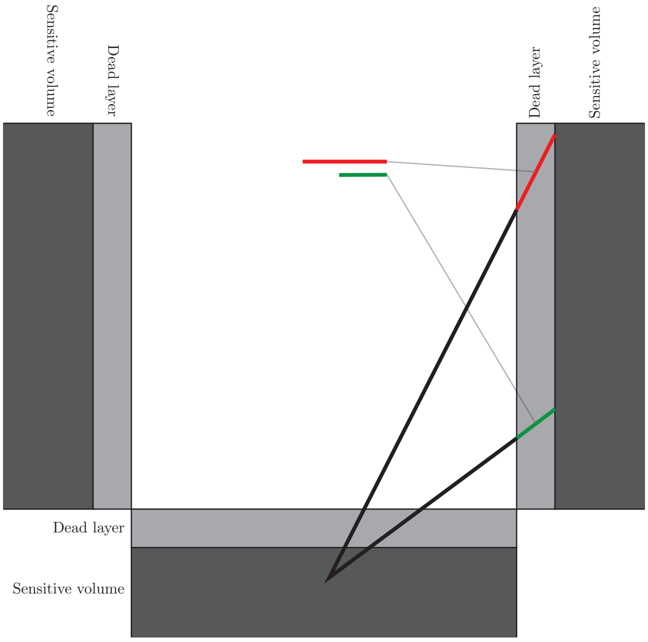

Figure 24: Two different particle trajectories which experience different effective thicknesses. The thickness of the dead layer is obviously exaggerated to visualize the effect.

This can, however, be remedied. If we assume that the particle originates from the center, which is a reasonable assumption since the particles are focused such that they hit as close to the center of the implantation detector as possible, the spatial information provided by the DSSSDs allows for the calculation of the incident angle. By knowing the actual thickness of the dead layer, the effective thickness can be calculated, thereby allowing for the estimation of the energy loss which can be used to find the incident energy of the particle.

A more precise method could use the signal from the implantation detector to determine the origin of the alpha particle, thus obtaining a more accurate effective thickness. The assumption of a point source in the center of the implantation detector, however, is significantly easier to implement, and is sufficiently accurate for the relatively simple dead layer correction (DLC) used here.

In practice the correction is done by having an array which contains the effective thickness, de, of each pixel. In order to calculate the energy of the particle before passing through de of dead layer, simulations of the stopping power dE/dx is performed using SRIM [22]. By interpolating between these values, an estimate for all stopping powers between 0 and 20000 keV can be found, as can be seen in figure 25.

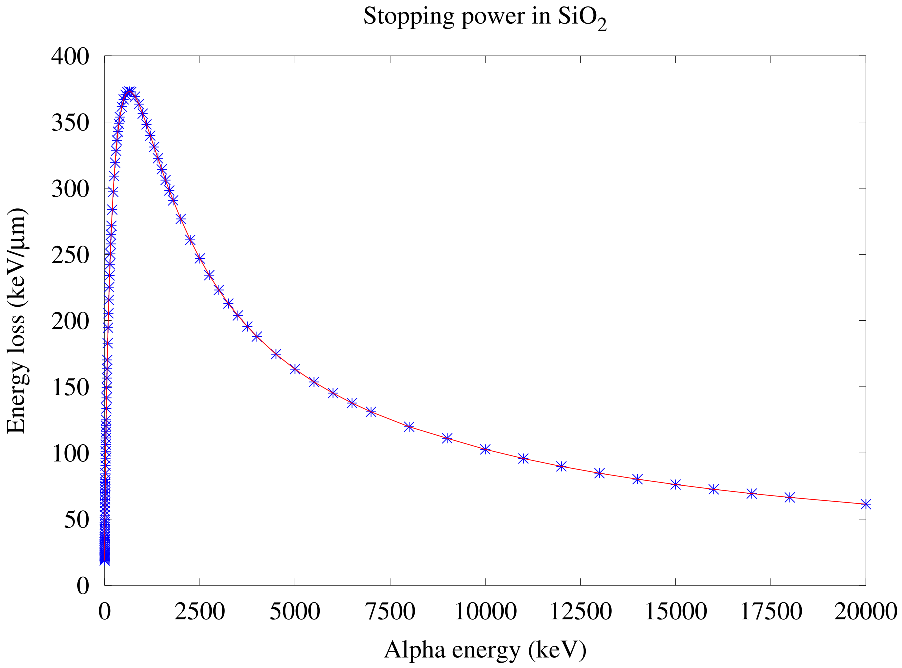

Figure 25: The stopping power obtained from SRIM are marked with blue stars. The red line represents the interpolation used to estimate the stopping power for all energies between 0 and 20000 keV.

Thus, the energy remaining after 1 μm can be calculated within this energy range. This is, however, quite large compared to the dead layer, which is on the order of a few μm. Because of this, smaller steps, with widths denoted as Δx, are used to increase the resolution. This is is the basis for an array consisting of the incident energy, E, corresponding to a registered energy E_r, i.e. the array contains E on position E_r. For instance, if the detector registers 5600 keV, the value of the array on this position is checked. If the particle lost 200 keV when passing through Δx of dead layer, the array contains 5800 on position 5600.

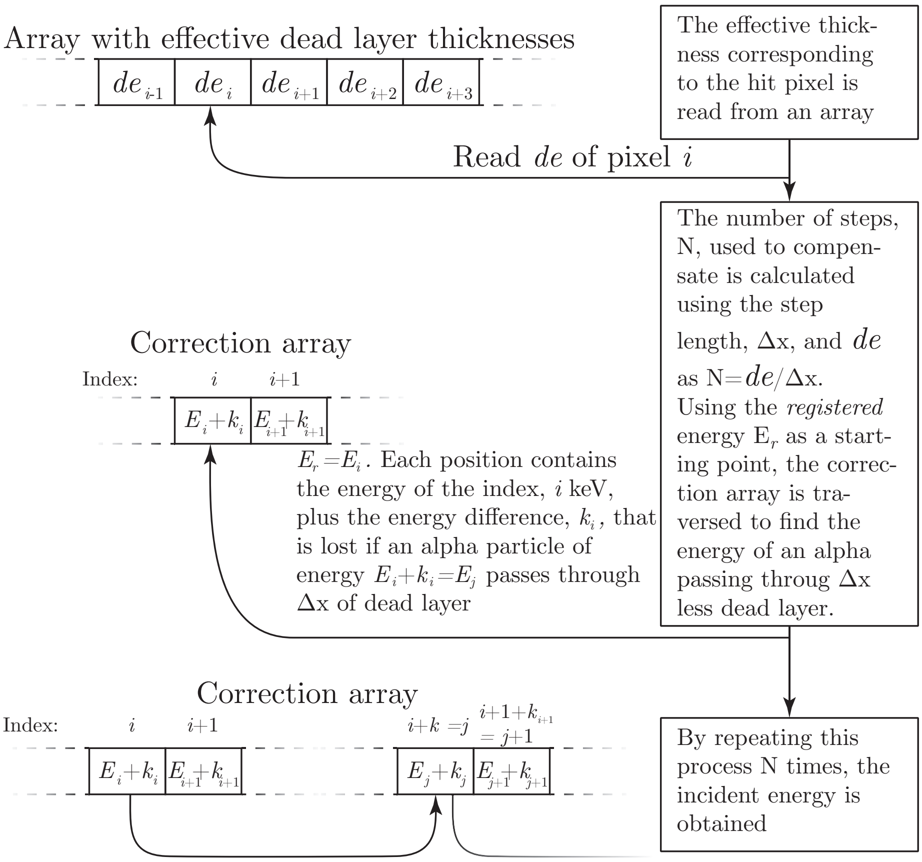

Figure 26: An illustration of the principles behind the DLC.

If the effective dead layer is $de \cdot \mu$m thick, the array is traversed $\frac{de}{\Delta x}$ times to find the incident energy of the particle. The process is illustrated in figure 26. This allows for a significant increase in energy resolution of the box detectors. In figure 27 one can clearly see the peaks spreading out towards lower energies in the uncorrected spectrum in figure 27(a), due to the different effective dead layers compared to the corrected spectrum shown in figure 27(b).

In order to get the best possible result of the dead layer correction (DLC), there are a few parameters that need to be optimized. The result in 27(b) is obtained assuming a dead layer consisting of a 1.8 μm thick layer of SiO_2, where the source is placed at $(0, 0, -86)$mm, if the origin is defined as the center of the surface of the implantation detector. The correction array uses steps of length 0.05 μm. These values, based on measurements of the distance from the implantation detector to the calibration source and a rough estimation of the dead layer, might not be optimal. Thus, it is conceivable that by tweaking these, the energy resolution might be improved further.

The *step length* needs to be appropriately long compared to the other values. Taking large steps saves on computation, but decreases the resolution of the

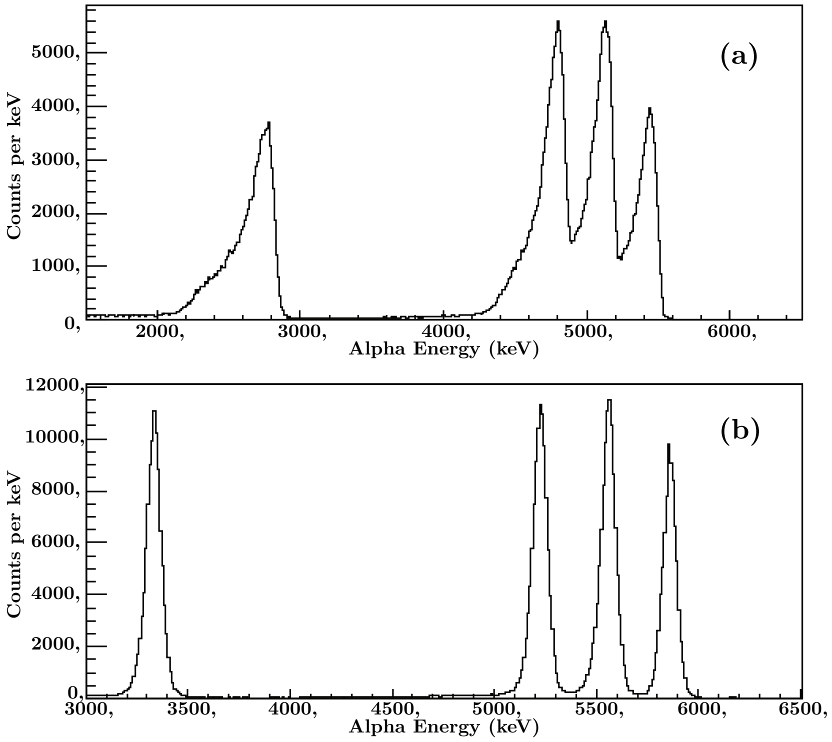

Figure 27: A comparison between box spectra from a 4-line α-source with and without dead layer correction. (a) The total projection of one of the box detectors using traditional calibration. (b) The same spectrum using dead layer correction.

effective dead layers, as this is just multiples of the step length.

To short a step length will become an issue with regards to two things: Firstly, the obvious disadvantage is the increased amount of operations needed to correct for the energies, resulting in slower data sorting. The second, and less obvious, problem is related to the correction array. Since this uses a resolution of 1 keV, too short a step length will result in energy steps that are small compared to this energy. Thus, the relative error of each step will increase, resulting in a decreased obtained energy resolution.

To find an appropriate Δx, the step length was varied, while keeping the other variables fixed at the values given above. The source used for these tests is a 4-line α-source consisting of ^{148}Gd (3.27 MeV), ^{239}Pu (5.16 MeV), ^{241}Am (5.48 MeV) and ^{244}Cm (5.80 MeV) (energies from Table of Isotopes, vol 2, [23]). Using the fitting tool available in GO4, the four peaks were fitted to a Gaussian peak in order to determine their width.

From table 2, it is apparent that the best energy resolution is obtained by using 0.05 or 0.1 μm steps, with the mean peak width being slightly smaller for 0.1 μm. The resulting spectra can be seen in figure 28. The drop in resolution is more apparent for very small steps compared to the longer ones.

The next step was to determine if changing the detector geometry could decrease peak widths by altering the thickness of the dead layer and the posi-

Table 2: Peak widths for varying step lengths. The smallest widths for each column is marked bold.

Step Length (μm)	Peak 1 σ (keV)	Peak 2 σ (keV)	Peak 3 σ (keV)	Peak 4 σ (keV)	Mean σ (keV)	Mean FWHM
0.01	52.6	67.5	47.9	64.4	58.1	136.5
0.02	42.7	41.6	42.2	42.6	42.3	99.3
0.05	**39.5**	39.3	39.9	**35.4**	38.5	90.5
0.1	41.0	**38.1**	**36.6**	37.1	**38.2**	**89.8**
0.2	42.3	40.6	40.0	39.1	40.5	95.2
0.5	51.9	47.7	45.9	43.2	47.2	110.9

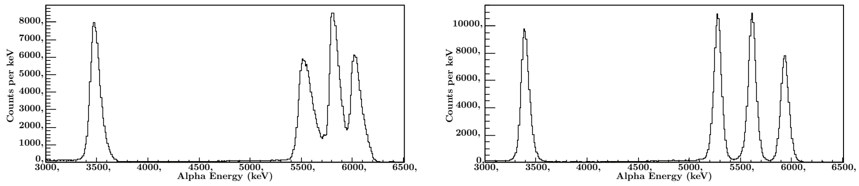

(a) 0.01 μm steps

(b) 0.02 μm steps

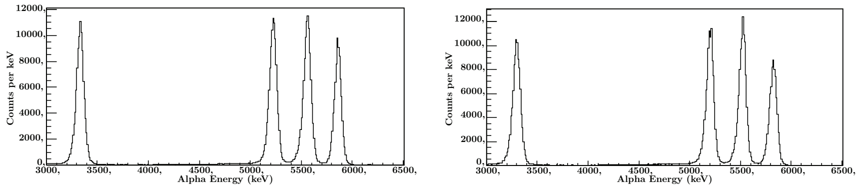

(c) 0.05 μm steps

(d) 0.1 μm steps

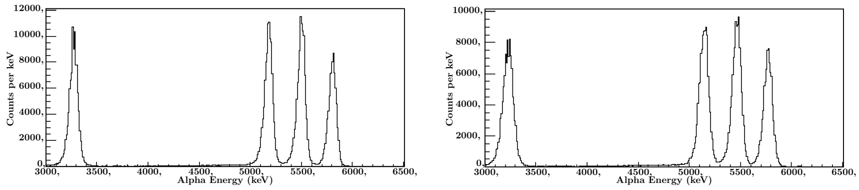

(e) 0.2 μm steps

(f) 0.5 μm steps

Figure 28: The six spectra resulting from different step lengths.

tion of the calibration source. The initial approach was to measure the standard deviation of the peaks for $\Delta z = 0, -5$ and $+5$ mm for the thicknesses $2.1, 2.0, 1.9, 1.8, 1.7$ and 1.6 μm using the GO4 fitting function.

The resulting contour plot in figure 29 shows that there is a valley of preferred values running from roughly 1.8 μm at $\Delta z = -5$ mm to 2.0 μm at $\Delta z = +5$ mm. This is reasonable, as moving the source closer to the implantation detector, i.e. a positive Δz, will result in smaller thickness factors and vice versa. Since the local minima lie on the edges of the plot, the data set was expanded with six new data points at $\Delta z = \pm 7$ mm, resulting in figure 30.

Using a cubic spline interpolation of the expanded data set was performed in an attempt to find the optimal geometrical parameters. The resulting figure

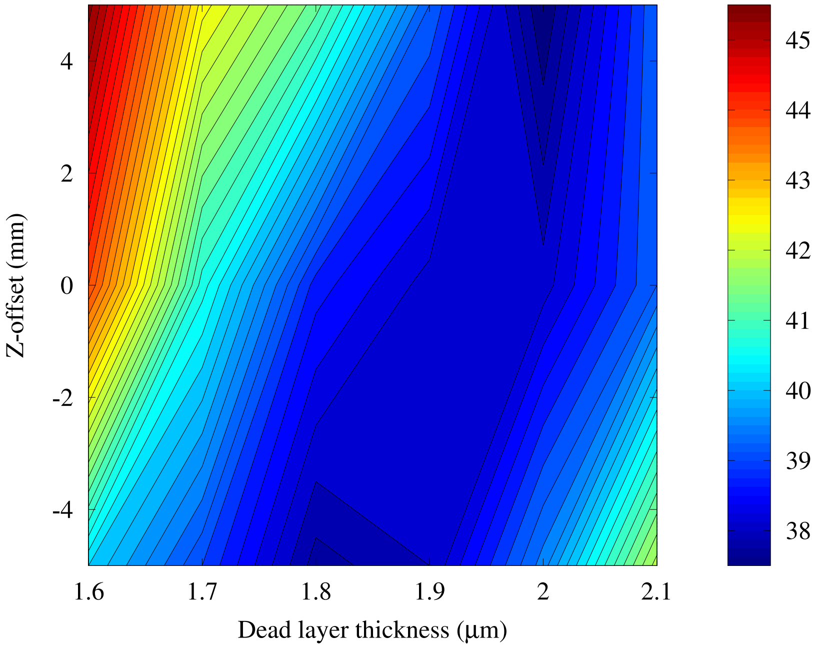

Figure 29: A contour plot of the standard deviation of the peaks with data points at $\Delta z = 0, -5$ and $+5$ mm, $2.1, 2.0, 1.9, 1.8, 1.7$ and 1.6 μm.

31 suggests that the smallest peak width should be found around 2.0 μm with $\Delta z = 3.7$, followed by 1.8-1.9 μm with $\Delta z = -3.5$.

The mean peak widths of these values were tested, with the results available in table 3. These values are slightly wider than the best of the mean widths in the data set. Also, the predicted global minimum at $\Delta z = 3.7$ was larger than the local minimum at $\Delta z = -3.5$, suggesting that the interpolation is not sufficiently accurate. An attempt to remedy this was made by obtaining further data points at $\Delta z = \pm 2.5$, resulting in figure 32 and 33. The changes are not dramatic, but the minima are somewhat shifted towards the edges of the plot.

Table 3: The standard deviation of the peaks at the minima suggested by figure 31.

Δz (mm)	Thickness (μm)	Mean σ (keV)
+ 3.7	2.0	37.9
- 3.5	1.8	37.6
- 3.5	1.9	37.7

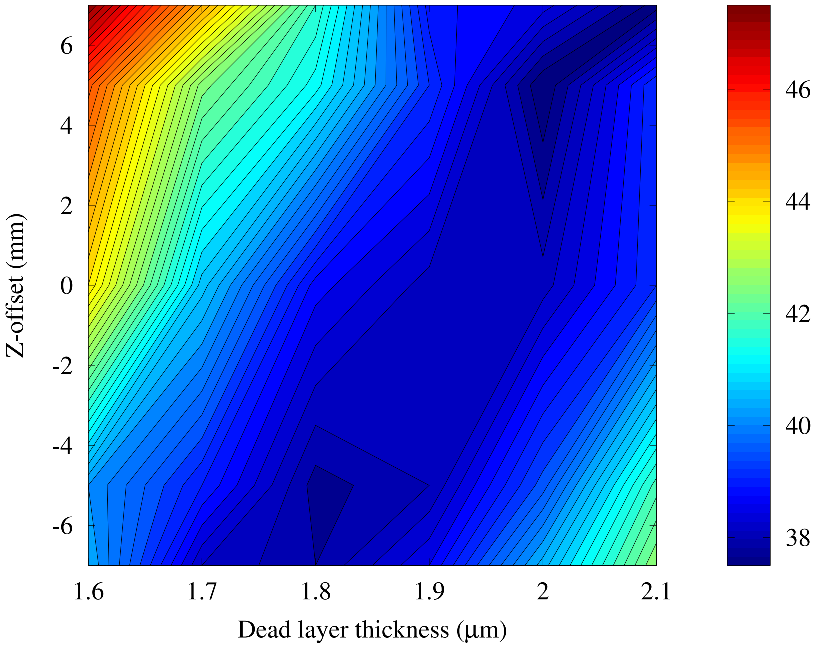

Figure 30: Expanded data set compared to figure 29.

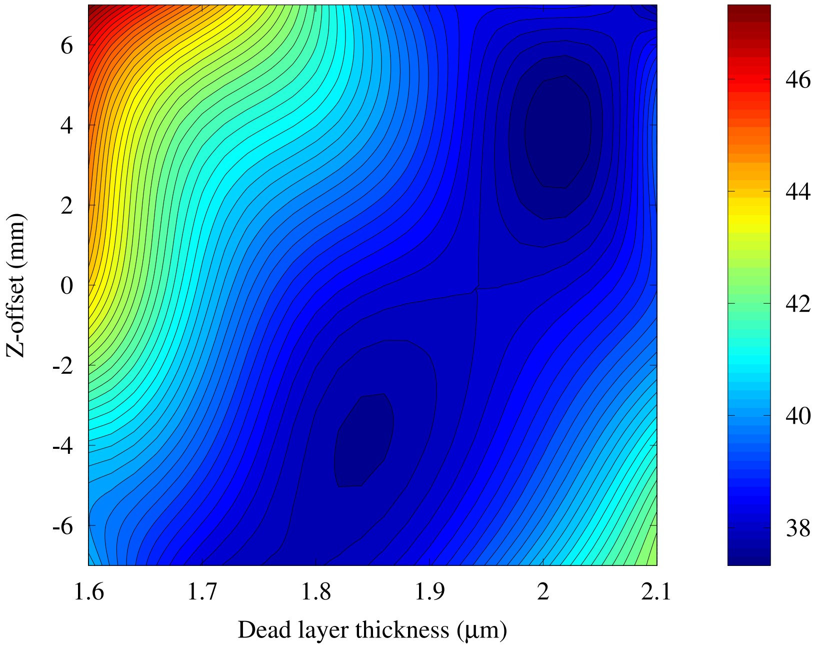

Figure 31: A cubic spline interpolation of the data set in figure 30.

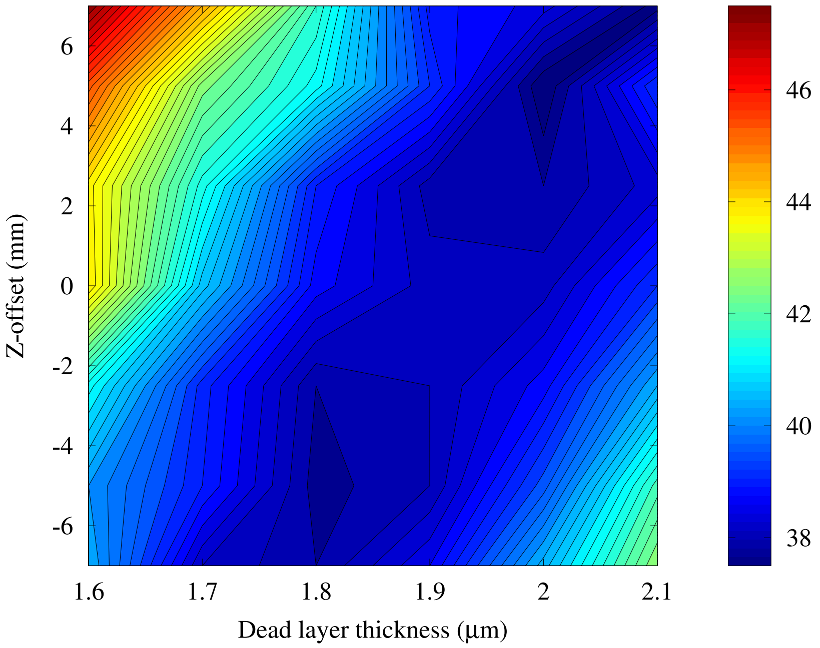

Figure 32: The contour plot using additional data points at $\Delta z = \pm 2.5$.

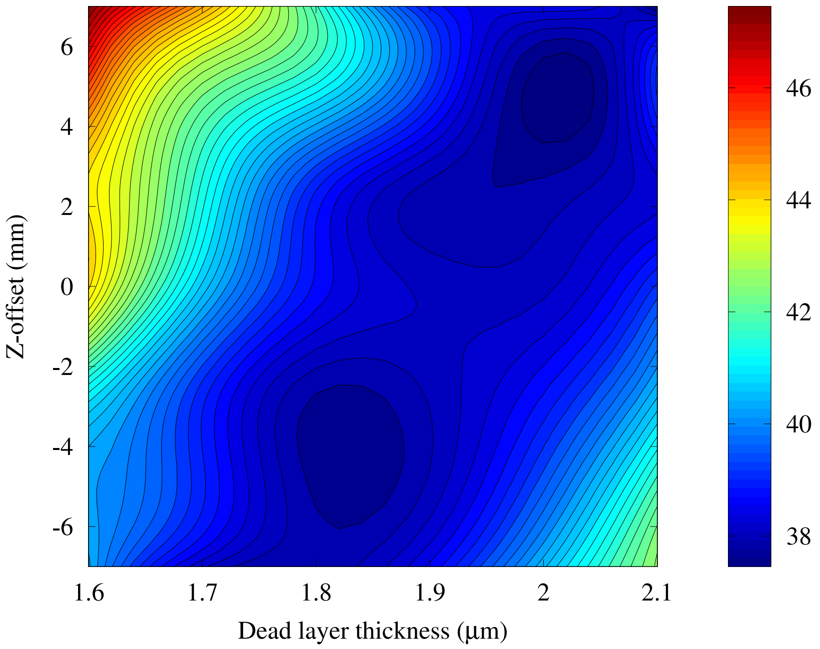

Figure 33: The cublic spline interpolation of figure 32.

New measurements of mean σ at the minima in figure 33 were performed, resulting in table 4. Once again, there was no significant improvement.

Table 4: The standard deviation of the peaks at the minima suggested by figure 33.

Δz (mm)	Thickness (μm)	Mean σ (keV)
+ 4.9	2.0	37.6
- 4.0	1.8	37.8

One would expect incorrect parameters to result in over- and under-compensation of the dead layer, leading to skewed peaks. This is confirmed when comparing a spectrum from the valley ($t = 1.9\mu$m, $\Delta z = 0$) to spectra from the corners of the contour plot ($t = 2.1\mu$m, $\Delta z = -7$ mm and $t = 1.6\mu$m, $\Delta z = +7$ mm) shown in figure 34. It is apparent that the $t = 2.1\mu$m, $\Delta z = -7$ mm slants the peaks towards higher energies, which is expected as this represents the thickest effective dead layer. The opposite is true of the spectrum for $t = 1.6\mu$m, $\Delta z = +7$ mm.

In light of this, it would seem reasonable to attempt to differentiate the peaks along the preferred valley using the peak shape, as the fitted peak width seems unable to do so reliably. The peaks of the two minima in figure 33 is shown in figure 35, and as can be seen, the shapes of the peaks are nigh indistinguishable. Even when superimposing the two peaks, as in figure 36, the peaks are practically identical.

The internal structure resulting in slanted peaks, such as in figure 34, can be seen more readily by looking at superimposed pixel spectra. By choosing pixels along a p-strip, inaccurate DLC-parameters will shift the peaks, resulting in a slanted peak as the spectra are summed up. This can be seen in figure 37, where five pixels have been chosen equidistantly along a central p-strip of the first box detector. As the solid angle is smaller for the pixels farther from the source, the amplitude of the peaks grows with increasing n-strip numbers. When the estimated thickness is too large, as in 37(b), the pixels on the earlier n-strip will shift their peaks to higher energies as the DLC overcompensates, which results in the black peak (the first n-strip) is shifted to the right of the light blue peak (the last n-strip). The opposite is true when the estimated dead layer is too thin, as can be seen in 37(c).

Using this approach to differentiate between the two sets of parameters in figure 35 results in figure 38. Both plots look promising as the peaks line up well for both geometries. Once again, however, there is little discernible difference between the two situations. The peaks were therefore fitted, and the difference between the positions calculated for the two minima as well as the point $\Delta z = 0$mm, 1.9μm at the center of the preferred valley. The inconclusive results can be seen in table 5, where the difference in position varies from positive to negative, despite the geometry being symmetric around the division between strip 8 and 9.

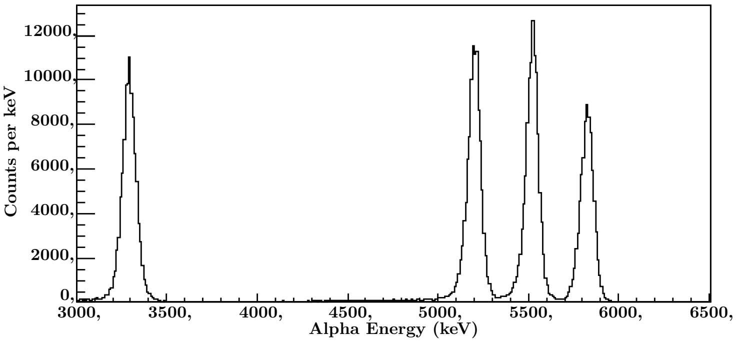

(a) $t = 1.9\mu m, \Delta z = 0$

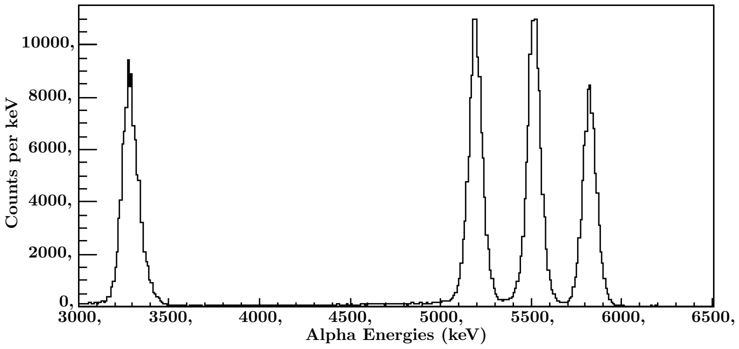

(b) $t = 2.1\mu m, \Delta z = -7$ mm

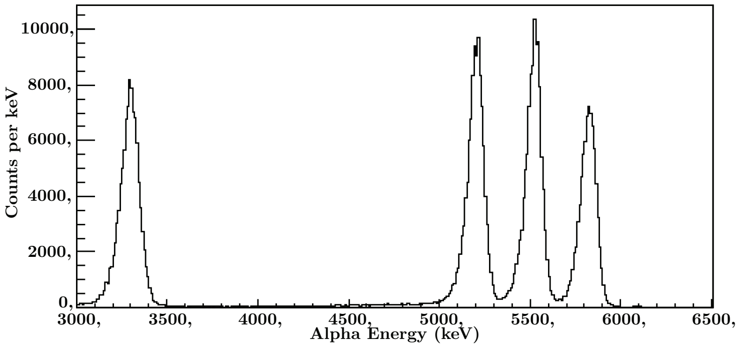

(c) $t = 1.6\mu m, \Delta z = +7$ mm

Figure 34: A comparison of peak shapes for a value from the preferred valley compared to undesired values of the corners of the contour plot.

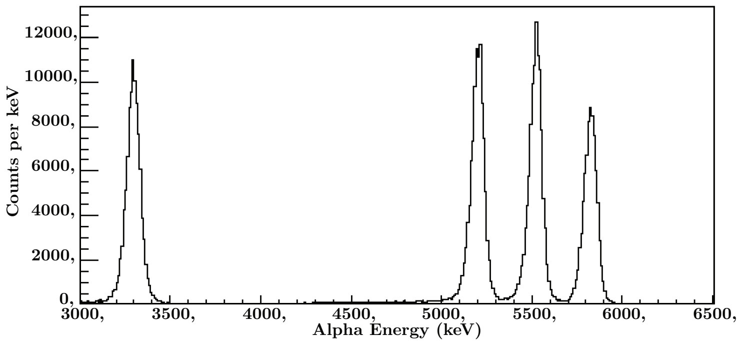

(a) The local minimum at $t = 2.0\mu m, \Delta z = +4.9$ mm

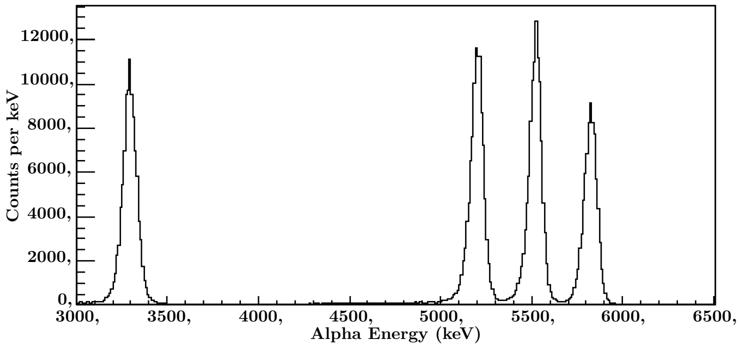

(b) The local minimum at $t = 1.8\mu m, \Delta z = -4$ mm

Figure 35: A comparison of peak shapes for the minima of figure 33.

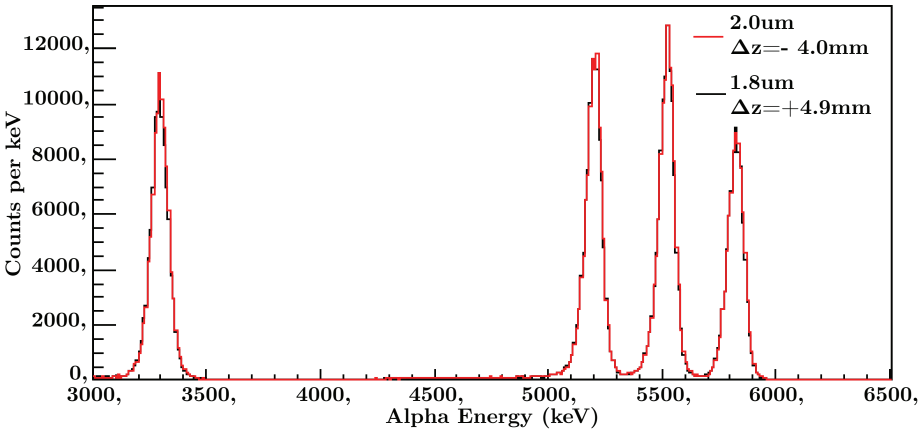

Figure 36: A superposition of the peaks in figure 35.

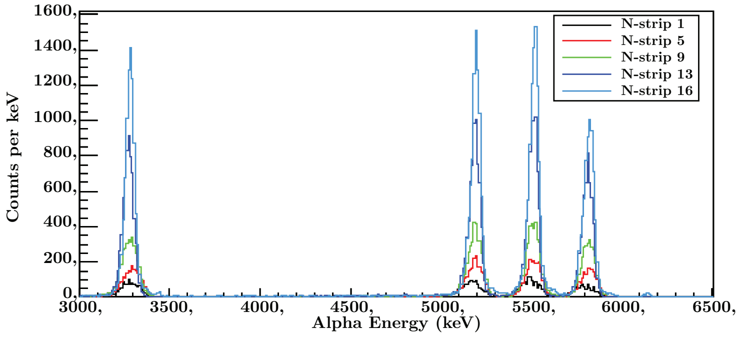

(a) $t = 1.9\mu m, \Delta z = 0$

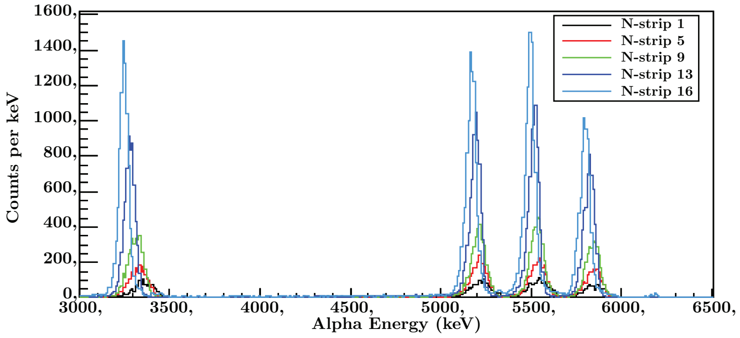

(b) $t = 2.1\mu m, \Delta z = -7$ mm

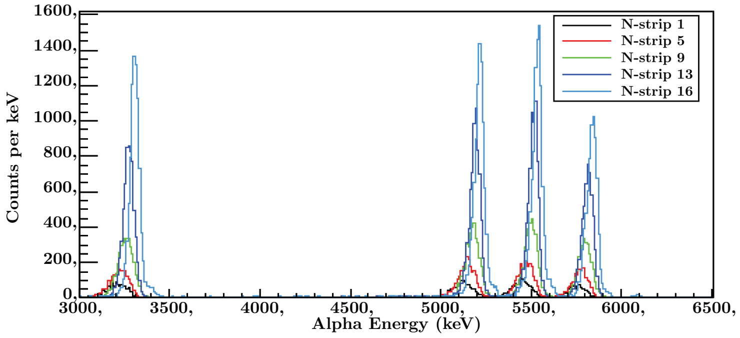

(c) $t = 1.6\mu m, \Delta z = +7$ mm

Figure 37: Superimposed pixel spectra corresponding to the plots in figure 34. The pixels lie on a central p-strip.

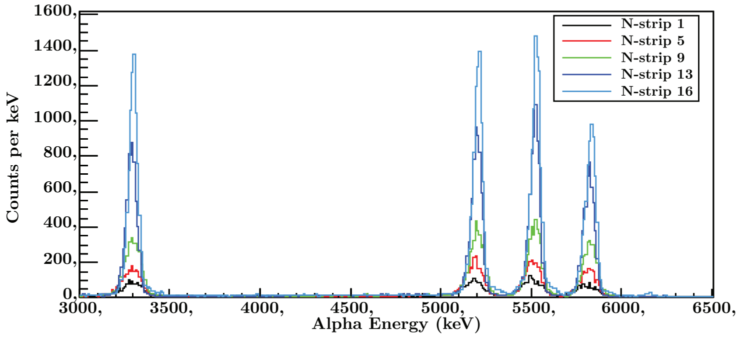

(a) The local minimum at $t = 2.0\mu m, \Delta z = +4.9$ mm

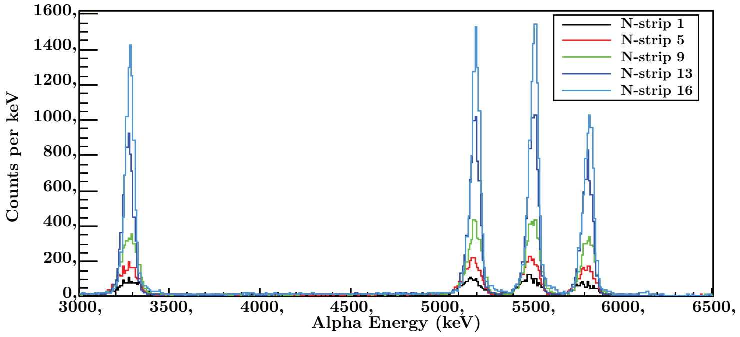

(b) The local minimum at $t = 1.8\mu m, \Delta z = -4$ mm

Figure 38: Superimposed pixel spectra of the two minima of figure 33.

Table 5: The peak separation between the first and fourth n-strip for four pixels positioned on the four central p-strips.

Geometry	P-strip	Diff peak 1 (keV)	Diff peak 4 (keV)	Mean deviation (keV)
Δz = -4mm, 1.8μm	7	1.4	-21.1	**11.3**
Δz = -4mm, 1.8μm	8	**-5.3**	-25.3	**15.3**
Δz = -4mm, 1.8μm	9	-8.7	-27.1	17.9
Δz = -4mm, 1.8μm	10	**-6**	-22	14
Δz = 0mm, 1.9μm	7	1.4	-21.7	11.5
Δz = 0mm, 1.9μm	8	**-5.3**	-25.5	15.4
Δz = 0mm, 1.9μm	9	14	**-11.7**	**12.9**
Δz = 0mm, 1.9μm	10	14.4	-6.7	**10.6**
Δz = 4.9mm, 2.0μm	7	**0**	**-20.7**	10.4
Δz = 4.9mm, 2.0μm	8	-5.6	**-24.1**	14.9
Δz = 4.9mm, 2.0μm	9	**-6.4**	-26.1	16.3
Δz = 4.9mm, 2.0μm	10	16.2	**-6.6**	11.4

Thus, there are several combinations of geometry factors resulting in roughly the same mean peak width. The corresponding plots for all individual peaks have two minima at roughly the same place as figure 33, which is somewhat discouraging. The peak separations provide no further insight, as the difference in peak position vary with an unsystematic nature. This seems to indicate that there is some other factor which produces an error larger than the resolution of the DLC. Thus, there could be several parameter combinations which produce results with better accuracy, which is then smeared by this superimposed error.

The existence of the long valley of preferred values indicates that the influence of the z-coordinate has little influence on the energy resolution. The measurements of the source position suggesting that $z = -86$ are well within the tested ±7 mm and there is no discernible difference between the peak distributions of figure 38 with $z = +4.9$ mm and $z = -4$ mm.

The inability to find a definite minimum might indicate that some of the assumptions of the DLC-model is incorrect. If the model is correct we would expect to see a more prominent minimum as we get closer to the 'correct' geometry while moving along the valley in the contour plots. The dual minima of the mean plot could be explained as being the optimal factors for the two groups (one for the 3.27 MeV peak and one for the three peaks above 5 MeV). If this was the case, however, we would expect the one minimum to be more prominent for peak 1, and the other more prominent for the remaining three peaks. This is not the case, as can be seen in figure 39, where both minima are roughly equal for all four peaks.

This method assumes a dead layer of equal thickness for the entire detector. If this assumption is false, this method will over and under compensate for the dead layer in different areas, which might shift the spectra from different strips from their correct position. This might explain the difficulty in finding an optimal set of reasonable parameters.

In order to obtain a better energy resolution, a more advanced approach will probably have to be taken, as further tweaking of this method is unlikely to be fruitful. Still, this method is relatively simple to set up, and provides a significant resolution boost, clearly visible in figure 27. It can thus be used for online analysis where computational complexity and speed outweigh optimal accuracy in importance.

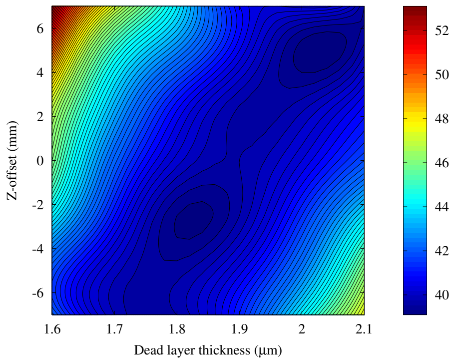

(a) Peak 1

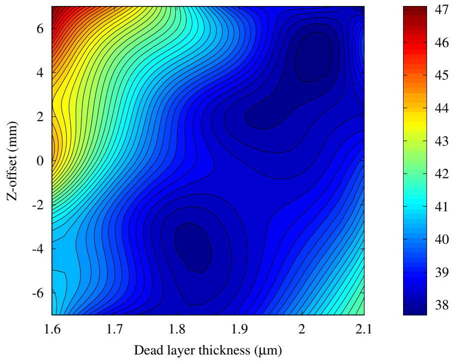

(b) Peak 2

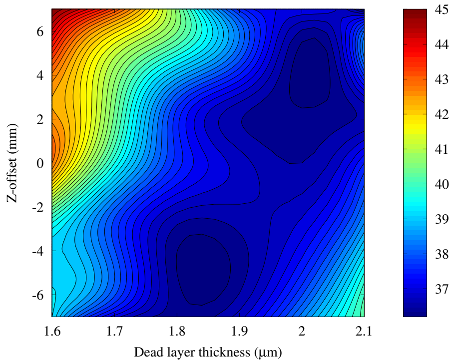

(c) Peak 3

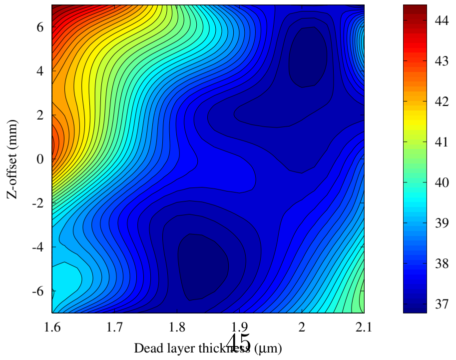

(d) Peak 4

Figure 39: The contour plots for the four peaks.

3.2 Mesytec ADCs

In addition to the new box detectors, all of the silicon detectors were upgraded with new ADCs made by the company Mesytec. These offered a few different settings with respect to the energy resolution, which were tested to determine which is preferable.

Firstly, there is the option of setting the number of digital channels used in the conversion. This can be set to 2048 channels (2k), corresponding to 11 bits, 4096 (4k), corresponding to 12 bits and 8192 (8k), corresponding to 13 bits. In addition to this, the 4k and 8k options offer a 'hires' setting which claims to have a lower channel noise, at the cost of doubling the conversion time, resulting in a longer dead time for the data acquisition system (DAQ).

Choosing a setting is a compromise between a few different factors. Obviously it is desirable to have the best possible energy discrimination, which implies that one of the 8k settings is the best option. However, since the detector set-up has an inherent energy resolution, using an ADC resolution much higher than this will not improve the measured resolution. On the other hand, the conversion time increases with the ADC resolution, meaning that the insensitive time after each event is increased, thus decreasing the maximum event rate that the DAQ can handle.

The modes were compared in Lund using a ^{228}Th source. Spectra were collected from a central p-strip of the implantation detector using the five different settings. The ADCs had an input range of roughly 0-20 MeV. The result can be seen in figure 40 and table 6. Note that the lowest peak of the ^{228}Th spectrum is cut off due to a threshold.

Table 6: The fitted FWHM for the 6.906 MeV peak of the ^{228}Th spectrum.

Setting	FWHM (keV)
2k	72.9
4k	72.6
4kH	70.5
8k	72.9
8kH	70.7

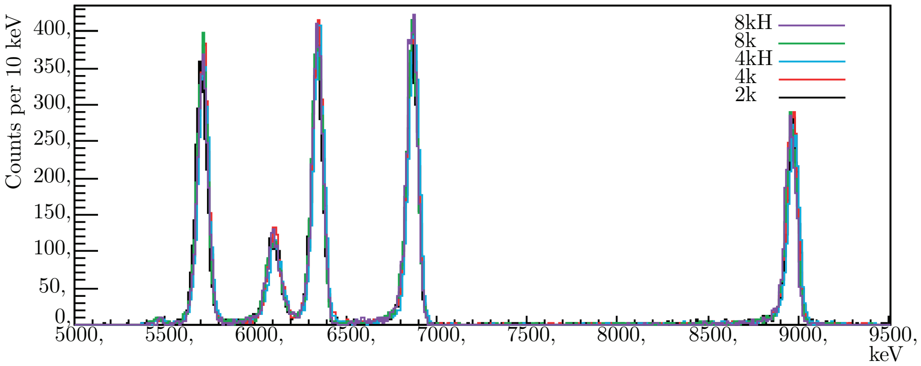

Figure 40: The spectra produced with the five different ADC settings

The differences between the peaks are subtle and cannot be made out visually. 2k, 4k and 8k seem to produce the same result considering that the fitting function estimates the error of the fitted widths to be of the order of 1 keV. This appears to suggest that the limiting factor here is not in the number of bits used for the conversion. A range of 0-20 MeV means that at 2k, each channel represents roughly 10 keV, which obviously is sufficient not to degrade the quality of peaks of this width.

The hires settings, however, appear to have a small positive effect on the peak widths. Both 4kH and 8kH provide practically the same width, but slightly better than the non-hires peaks.

Since these alpha particles originate from outside the implantation detector, as opposed to the ones emitted from an implanted EVR, the dead layer will affect them. The difference in energy loss, however, will be significantly smaller due to the smaller differences in incident angle for the pixels of the implantation detector compared to the box detectors. Still, it might be conceivable that this small effect might mask the difference between the settings, and thus a test with the DLC described in the previous section adapted for the implantation detector was performed. The results are shown in figure 41 and table 7.

Table 7: The fitted FWHM for the 6.906 MeV peak of the ^{228}Th spectrum using DLC for the implantation detector.

Setting	FWHM (keV)
2k	71.0
4k	69.8
4kH	67.4
8k	69.6
8kH	67.4

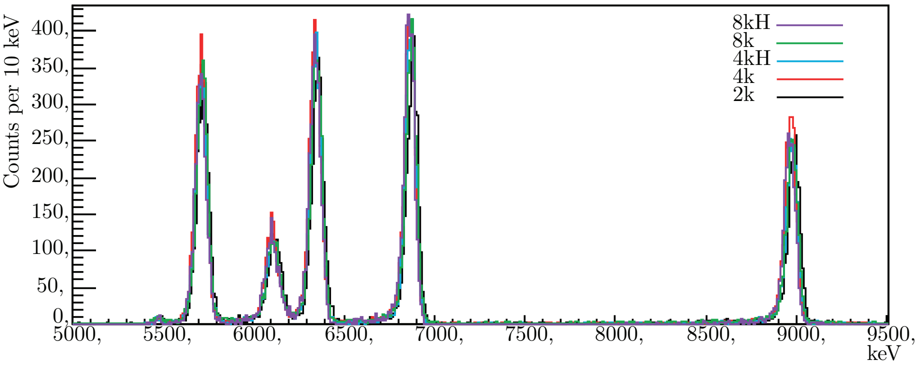

Figure 41: The spectra produced with the five different ADC settings with DLC for the implantation detector

The DLC resulted in somewhat narrower peaks, as suspected. However, the difference between the modes remained roughly the same. The difference between 2k compared to 4k and 8k is somewhat larger which might suggest that 2k is at the limit when it comes to resolving the peak accurately, but the effect is still close to the estimated error of roughly 1 keV. Once again, the hires modes performed equally well and somewhat better than the non-hires modes.

In previous experiments, 4k has been used, since the resolution of 5 keV per channel has been deemed sufficient for resolving the peaks, and since the conversion time is half that of 8k. Is seems that there is still no reason to use 8k over 4k, at least not with peaks of this width. It might, however, be worth considering using 4kH, as it seems to provide an improved resolution. This has to be weighed against the doubled conversion time resulting from using the hires mode, and thus depend on the expected count rate of the system. This, in turn, depends on how well the suppression of the background of non-interesting nuclei making it through TASCA works, as this is the main contribution to the count rate of the system.

4 Beam Shut-off

The beam structure used at GSI has, as described previously, a duty cycle of 25 %, meaning that the macropulse is present for 5 ms of the 20 ms cycle. During this period, known as *beam-on*, the beam particles hit the target. This results in a significant increase in background compared to the *beam-off* period. This is clearly demonstrated in figure 42, where the larger peaks in the beam-off spectrum can still be hinted in the beam-on spectrum, while the smaller peaks, clearly visible in the beam-off spectrum, disappear completely in the beam-on counterpart.

Since the identification of super-heavy elements is contingent on the detection of the expected decay chain, it is desirable to suppress the background to as large extent as possible during an interesting event. This is especially true for experiments with very heavy elements, such as the one involving element 115, where the cross sections are very low, and only a few atoms are created in experiments running for months. Thus, there should be no beam present during the nuclear decay of the atom. One decay chain, however, stretches over several macro pulses, meaning that the beam should be shut off for an appropriate amount of time when an interesting event occurs.

Previous SHE experiments at TASCA have not yet utilized such a feature. Instead, only events during beam-off were used. This meant that 25 % of the data is discarded, which is acceptable if the cross-sections are high enough. In preparation for the element 115 experiment, however, it was deemed that it would be beneficial to implement a shut-off routine as the yields for element 115 are on the order of a few atoms per week of beam time (see Section 2.1.1). The realization of this functionality was my main responsibility during the preparation for the experiment.

4.1 Element 115 version

In order to distinguish an interesting event from the vast amount of uninteresting ones, one must choose a signature that is present in all detected element 115 events and absent from the background to a sufficient degree. If the criteria are too accepting, valuable beam time will be lost as a result of false events triggering the shut-off.

One might consider using the energy registered when the element is implanted in the silicon detector. However, this energy is not strictly defined, and typically varies over a range from 12-17 MeV. Also other reaction products will have similar energies, making it hard to discriminate wanted events from unwanted ones.

Instead the alphas emitted in the decay chain are used. Figure 13 shows that the anticipated alpha-decay energies all lie between 9 and 11 MeV, which contains little background from alpha-decays of target-like particles, and is not in the energy range of the implantations. Only the implantation detector is considered, as the calculations necessary to perform the DLC cannot be run on the processing unit responsible for the readouts in the VME crate. This means that there is a 50% chance to detect any given alpha from the decaying nucleus due to the solid angle. This is not a problem, since the energies of the alpha particles lie within a relatively narrow range.

Every time the system is triggered, a readout routine is run by the processing

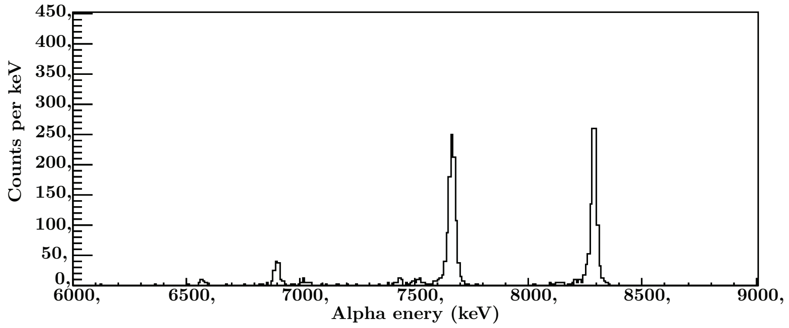

(a) beam-off

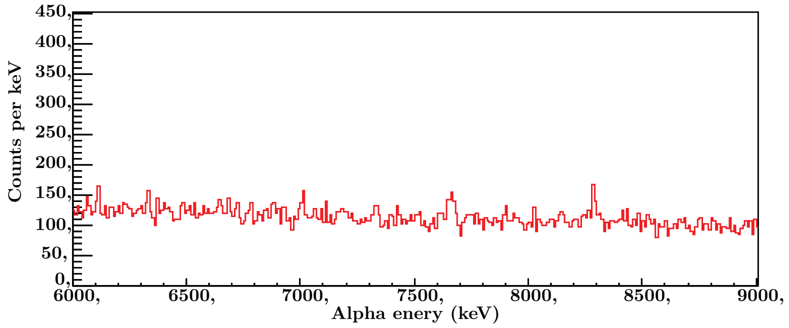

(b) beam-on

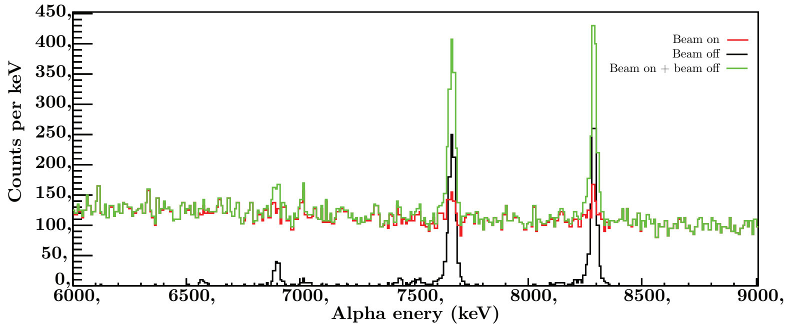

(c) beam-off and beam-on superimposed

Figure 42: Spectra for beam-on and beam-off for the reaction ^{48}Ca + ^{208}Pb $\rightarrow^{254}$No+2n, which also produces some transfer products, such as $^{211-212}$Po and ^{211}Bi.

unit in the VME crate. Here the user can define in what order the modules are read out and how they should be put together to form an event. This is done by writing the bytes in the correct order to a memory buffer referred to by a specific pointer. The shut-off routine is simply a subroutine that is run immediately after each readout of the p-side of the implantation detector. By doing this before the rest of the readout is performed, the shut-off is performed as quickly as possible.

This routine contains an array with the two constants used for a linear calibration for each ADC channel, as well as a bit (henceforth known as the

ABBA-bit) for the shut-off status. Using a pointer to the memory buffer containing the data that has been read out from the ADC, the triggered channel (if any) and amplitude is obtained. The amplitude is then translated into an energy, which is compared to the set thresholds corresponding to the interesting alpha energies.

Since the beam-on spectrum contains background over the entire energy range of interest, only events within the thresholds during beam-off trigger the system. This is checked using a status signal available from the UNILAC. This signal is high during the macro pulse and low the rest of the time. However, this pulse is fractionally smaller than the duration of the beam-on background. To make the pulse cover the entire beam-on period, the signal is split, and one of the signals is sent to a delay unit. The two pulses are then combined using a logical OR to create an elongated beam-on signal. This is sent to the pattern unit and is used by the shut-off subroutine to determine the beam status.

If both the energy and beam criteria are fulfilled, the ABBA-bit is set to one, otherwise it is left unchanged. In this way, all non-zero ADC channels are checked against the energy thresholds. After all channels have been read, the ABBA-bit is checked. If it equals 1, at least one channel has fulfilled the shut-off criteria.

The word `ABBA0001` is then written to the event buffer to indicate this in the data stream; otherwise `ABBA0000` is written. This has been chosen because it is distinct from other reserved words used by other modules (such as, for instance, `DEADBEEF` or `AFFEAFFE`), and because it is easy to spot in the data stream (and, somewhat less officially, to represent the Swedish contribution to this international collaboration). Afterwards, the ABBA-bit is reset to zero, and the routine is ready for the next event.

The physical shut-off is performed by sending a pulse via an output in one of the VME modules. This is fed through to a module which controls the *chopper*, which is the same method that is used to turn off the beam in case of loss of synchronization with the target wheel, too high detector rate, and a number of other parameters to ensure the safety of the experimental set-up. The chopper deflects the ion beam before it reaches the main part of the accelerator, which completely and immediately removes the beam from the cave. A flow diagram of the ADC readout with the shut-off active is show in figure 43.

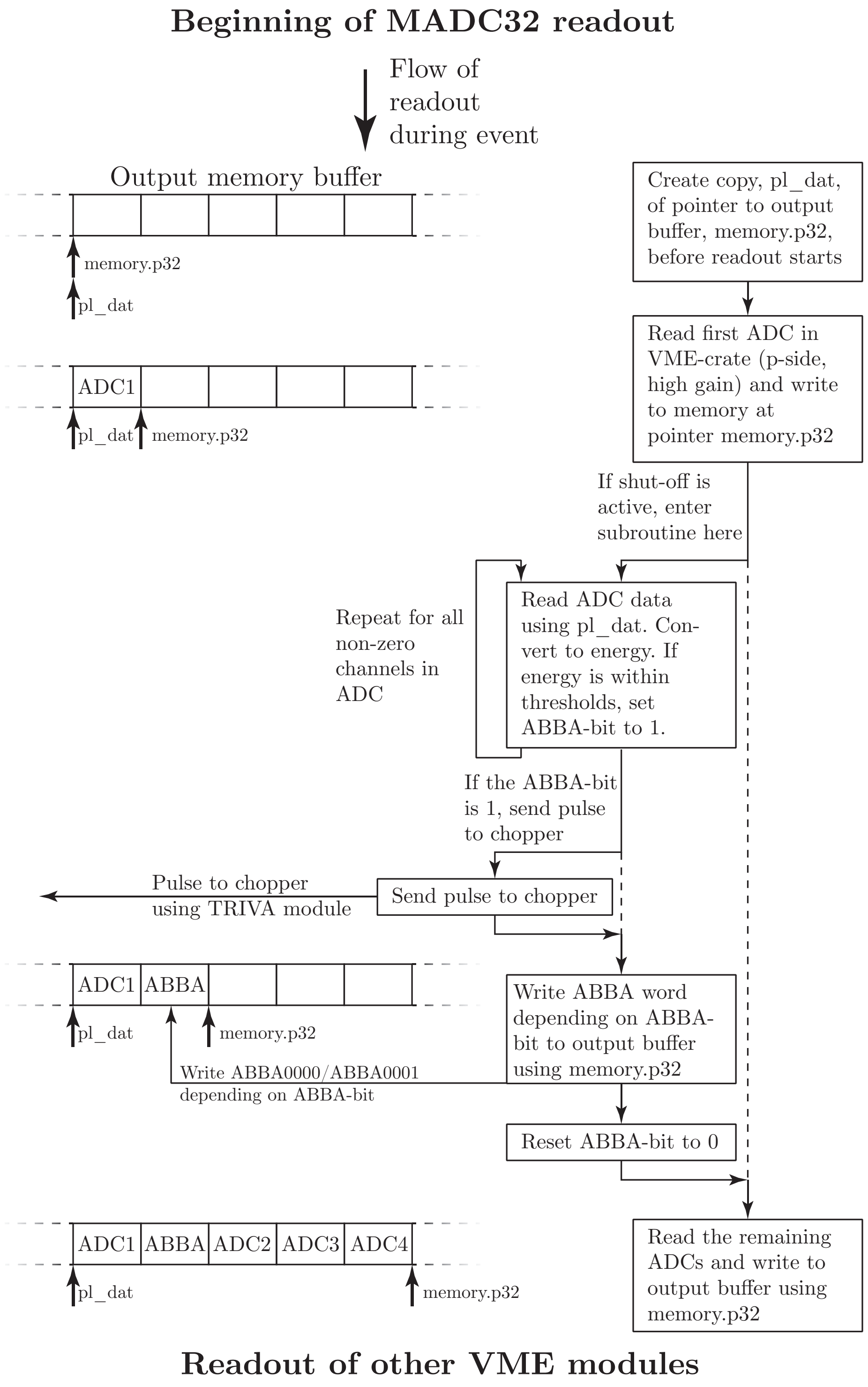

Figure 43: A flow diagram of the readout of an event with the shut-off active. Note that the ADC words are not necessarily of the same length, as this will depend of the number of channels triggered.

4.1.1 Initial Realization and Testing

The shut-off was first tested during the preparations in Lund, before the tests performed at GSI. This was done using a ^{241}Am source which emits 5.48 MeV alpha particles. Since there is no beam signal here, the only condition was the energy thresholds. These were set to trigger between 5.4-5.5 MeV, which should effectively represent one half of the peak. This is also what happened, as shown in figure 44, where the shut-off events clearly represent the desired energy range.

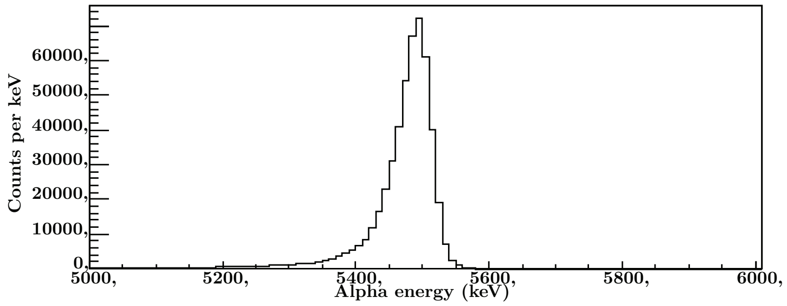

(a) The ^{241}Am peak without any conditions

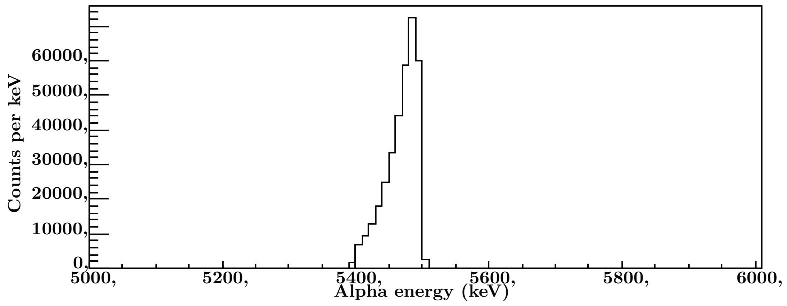

(b) The ^{241}Am peak, ABBA0001 only

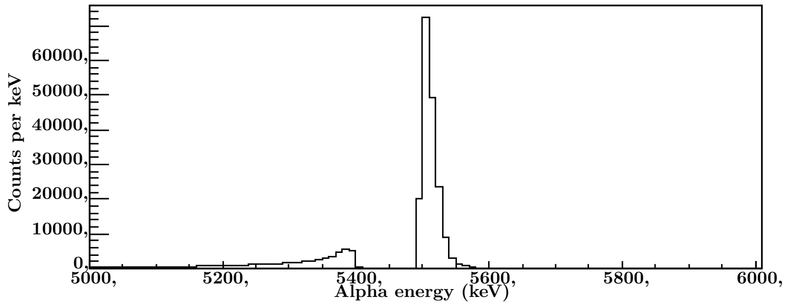

(c) The ^{241}Am peak, ABBA0000 only

Figure 44: A ^{241}Am spectrum with a shut-off energy window of 5.4-5.5 MeV. The set energies correspond to the energies of the triggered events when sorted, which implies that the energy window of the shut-off routine works.

However, further testing was needed to ensure that the system worked as intended under real experimental conditions at GSI. This was tested during a beam time in June 2010 with the purpose of preparing for the element 115 experiment. In light of the proposed decay schemes (cf. figure 13), the energy window was set from 9-11 MeV, and the set-up was connected to the chopper to verify that the shut-off routine could physically shut the beam-off. A ^{208}Pb target was irradiated with a ^{48}Ca beam to form ^{254}No through the $2n$-channel. This has a half-life of 55 seconds and decays through a 8.093 MeV alpha to ^{250}Fm. This in turn, decays to ^{246}Cf through a 7.430 MeV alpha. However, since this has a half-life of 30 minutes, it will only show up in small amounts during measurements of a few hours.

In addition to this, some transfer products positioned above and to the right of ^{208}Pb on the nuclide chart , such as $^{211-212}$Po and ^{211}Bi, also make it through the separator, which will contribute with additional peaks to the spectrum. One of these ^{213}At decays almost immediately ($t_{1/2}$ = 125 ns) and emits an alpha with 9.080 MeV energy. The amount of this isotope that reaches the implantation is very small, but considering that this energy region is relatively devoid of other peaks, it should be seen in the beam-off spectrum, and should be able to trigger the shut-off. The resulting spectra are shown in figure 45.

In both of the tests, the calibration seems to be able to provide good resolution of the energy window, as both spectra are cut very close to the set energy threshold. Each of the shut-offs corresponded to a chopper interlock. This suggests that the shut-off routine works as intended and is ready to be used for the element 115 experiment.

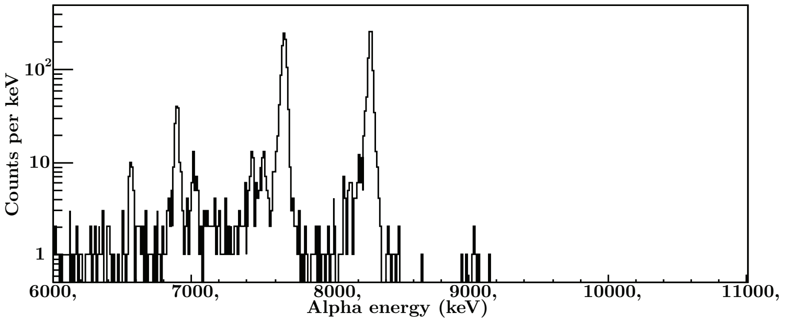

(a) beam-off spectrum without any conditions

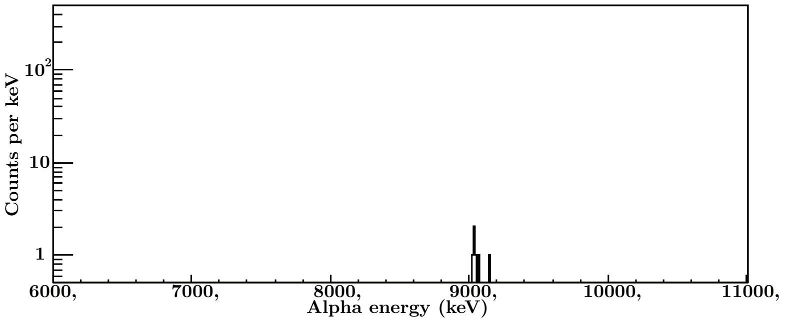

(b) ABBA0001 only

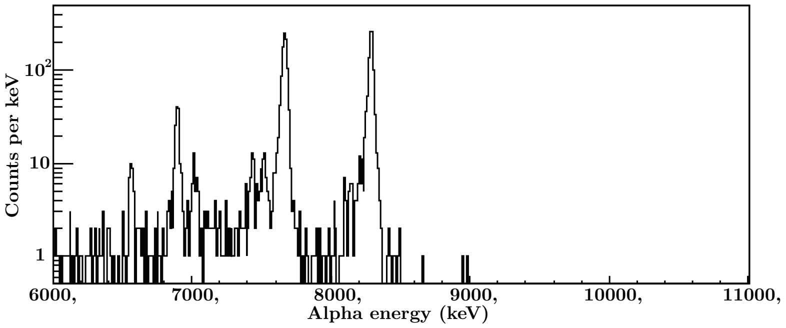

(c) ABBA0000 only

Figure 45: A spectrum of ^{48}Ca + ^{208}Pb $\rightarrow^{254}$No + transfer products. The shut-off is set to 9-11 MeV. The ABBA0001 spectrum only shows events in this energy range as expected.

4.2 Element 120 version

Since all elements up to $Z = 118$ have been discovered as of 2010, there is a lot of incentive to be the first to discover the next heaviest element. One experiment with the purpose of doing this intended to produce element 120 by irradiating californium with titanium, using the focal plane detector of TASCA to detect the EVRs. For this experiment, the shut-off routine was upgraded to a more sophisticated version, pre-designed by L.G. Sarmiento from Universidad Nacional de Colombia in Bogota, and fine tuned by myself, together with support from the DAQ experts at GSI.

The main difference from the element 115 version is a more advanced triggering scheme. Instead of relying on just one energy for the trigger, it uses two energy windows, thus taking advantage of the fact that a decay chain emits several consecutive alphas in a fixed position. Additionally, there is a time window within which the two registered alphas have to lie to trigger the shut-off. If this feature was not implemented, two unrelated events could easily set off the system.

A flow diagram of the upgraded shut-off routine is shown in figure 46. It might seem counter intuitive to start by checking the second energy window before the first one. The reason for this is that if the two energy windows overlap, which is often the case as the alpha particles have roughly the same energy, and if the registered energy lies within this overlap, the logic would not work as intended. The first window will cause the current time to be written to the array of time stamps, and as the second window causes the current time to be checked against the time stamp that was just written. This means that a single event that lies within this energy would trigger the shut-off every time, which is not how the routine should work. By reversing the order of the conditions, this problem is eliminated, as the time stamp is checked before it is written for any given event.

The strips of the focal plane detector are multiplexed in a way similar to the box detectors of TASISpec. In light of this, two versions were developed. One compared the energies and times on a strip basis, which requires the disentanglement of the ADC channels. The other version performed the comparisons directly on the ADC channels without disentanglement. The latter was eventually used, as it is faster than the more advanced version. It does, however, increase the risk of two unrelated events triggering the system.

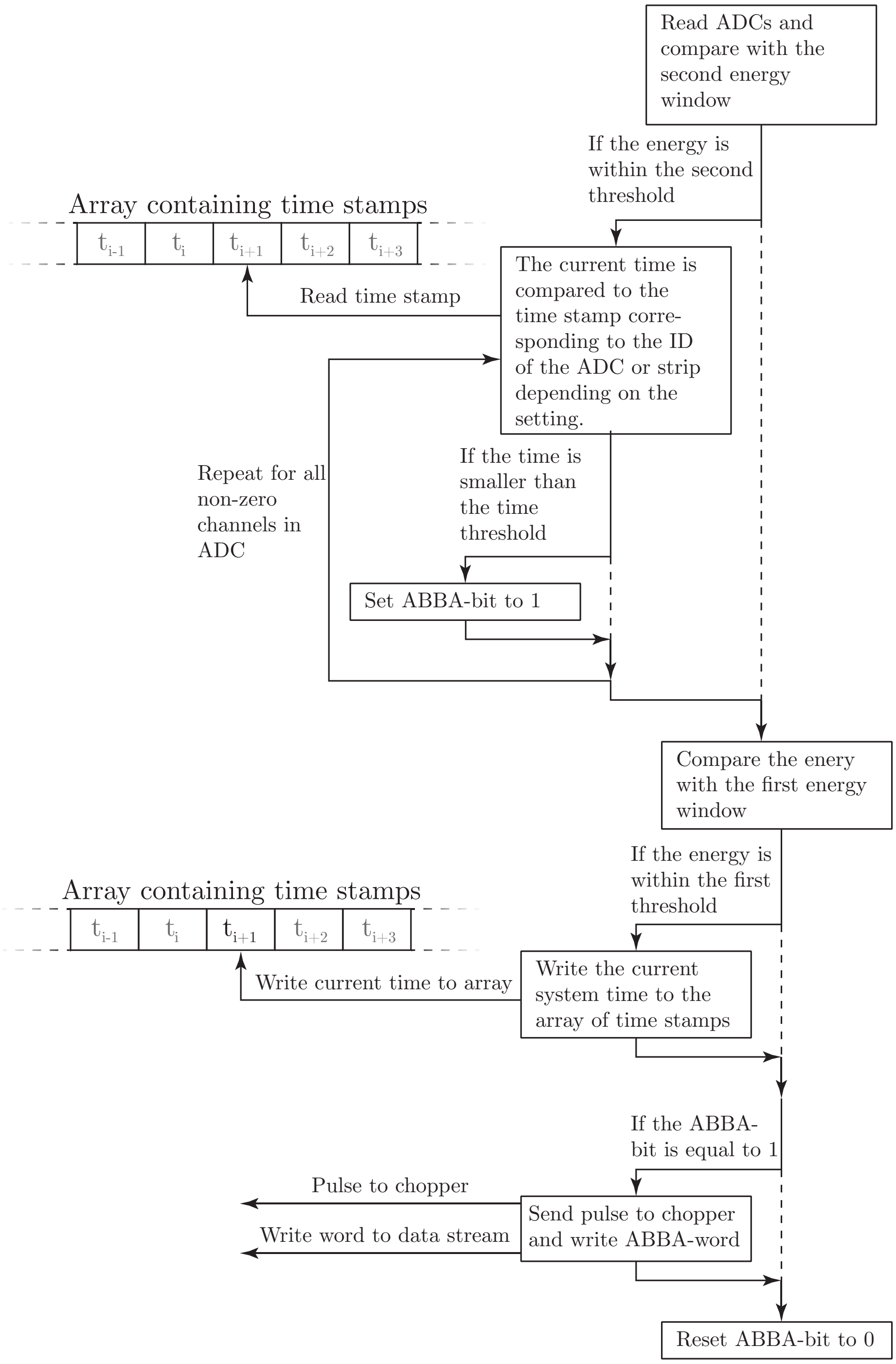

Figure 46: A flow diagram of upgraded shut-off routine used for the element 120 experiment. The second energy window is checked before the first to avoid a single event triggering a shut-off in case of overlapping energy windows.

The shut-off criteria was not chosen to correspond to two specific alphas in the chain. The reason for this is that there is only a 50% chance of registering a single alpha particle, due to the solid angle covered by a particle implanted in a planar detector. Thus, the probability of registering two specific alphas with full energy is only 25%. However, since the proposed decay chain of element 120 contains 6 alpha particles within a few milliseconds, the thresholds can be set to accept any pair within this chain. The probability of registering any two events in a chain of six is roughly 90%, assuming that the time window is long enough to cover the entire decay chain.

In the future it is conceivable to increase the chance of triggering on interesting events further by utilizing the beam status. During the beam-on period, the energy windows would then be set to correspond to an implantation followed by an alpha particle, and during the beam-off period, they would correspond to an alpha-alpha event. This is not used in the current version, which only looks for alpha-alpha chains.

This shut-off was tested using a pulser, which is a unit that sends two pulses with a given delay. The delay between the pulses was measured using an oscilloscope, after which it was sent to the ADCs. When the delay was shorter than the time threshold, the shut-off was triggered, indicating that the routine was working. It was used and working properly during the entire 8-week element 120 experiment in 2011.

5 Summary and Outlook

The proposed experiment searching for element 115 has been approved and given beam time. It was originally planned to be run during 2011, but this was eventually postponed to make room for an experiment with higher priority, searching for the hitherto undiscovered element 120. Instead, the 115 production run will likely be carried out during 2013.

TASISpec has been proven to work on previous experiments, as well as during the preparatory beam times carried out during 2011. The upgrades made to the box detectors have improved the resolution dramatically, which is evident from figure 27. The repeated attempts to improve the resolution further yielded little result, however.

It is evident that there is a relation between the z-coordinate of the source and the dead layer thickness with regards to peak width. This manifests itself as a valley in the contour plots, and is reasonable, since moving the source further away from the implantation detector will result in steeper angles with respect to the box detectors, which equates to a larger effective thickness. As long as the two variables stayed within this region, the resulting peak widths were practically identical.

This indicates that the relative difference in effective thickness between the various parts of the box detector is very small if the source is moved within reasonable amounts. However, even if the effect was small, one would still expect to see a gradual shift in peak widths. Since this is not seen, there might be some other non-systematic factors that are superimposed to the systematic loss in energy due to the varying thickness, which could hide these smaller variations. There have, for instance, been some indications that the dead layer is not equally thick for the entire detector, which it is assumed to be in this version of the DLC.

The new ADCs provided a few different resolution settings which were tested. These indicated that there is no gain in enery resolution from using 8k over 4k range. 4k has been used previously, and with a range of 0-20 MeV, 4k corresponds to 5 keV per channel when calibrated, which should be sufficient for all realistic peak widths. There is, however, some indication that it might be worth investigating the benefit of using the ”hires mode” in favour of the standard one, as these modes resulted better results for both 8k and 4k in both measurements. If it is decided to use this mode, it has to be verified that the resulting doubling of the conversion time, and consequently longer dead time, is not too long in comparison with the count rate of the system.

The beam shut-off system designed for the 115 experiment has been tested and worked as intended. The tests have verified that the real-time conversion to energy is sufficiently accurate, and that the signal used for the beam status only allows the subroutine to trigger on events during the beam-off period. The shut-off was also successfully able to engage the chopper when an event was detected.

All the components and factors needed to run the element 115 experiment have been tested and verified, and is ready to be used as soon as there is beam time available at GSI. This experiment is of great importance from a physics standpoint, perhaps even more so than searching for new decay chains, as any direct measurement of the proton number for these super-heavy elements is yet to be performed; something this experiment sets out to measure using characteristic X-rays.

Looking further ahead, heavier elements still are on the horizon. Oak Ridge National Laboratory is set to deliver roughly 20 mg of ^{249}Bk (berkelium) to GSI in March 2012, which is to be used as a target together with a ^{50}Ti beam to produce element 119. There are also plans to continue the search for element 120, which have alluded detection in all experiments so far. The discovery of these two elements will put some restraints on the order of magnitude of the production cross section for elements in this area, which will determine if it is possible to search for still heavier elements with similar reactions. If not, new approaches, such as radioactive beams might be needed to explore the island of stability further.

Regardless off what happens, the next few years are likely to be exciting for anyone interested in nuclear physics; the study of the building blocks of which everything is made.

6 References

[1] U. Kaldor and S. Wilson, "Theoretical chemistry and physics of heavy and superheavy elements". Kluwer Academic Publishers, 2003.

[2] Brookhaven National Laboratory. `http://www.nndc.bnl.gov/chart/`, January 2012.

[3] Y. Oganessian et al., "Synthesis of a New Element with Atomic Number $Z = 117$", *Phys. Rev. Lett.*, vol. 104, p. 142502, Apr 2010.

[4] Dagens Nyheter, "Sverige Hoppas På Berzelium." `http://www.dn.se/nyheter/vetenskap/sverige-hoppas-pa-berzelium`, November 2011.

[5] S. Hofmann, "Exploring the island of superheavy elements", *Physics*, vol. 3, p. 31, Apr 2010.

[6] V.I. Zagrebaev, "Fusion-Fission Dynamics of Super-Heavy Element Formation and Decay.", *AIP Conference Proceedings*, vol. 704, no. 1, pp. 31 – 40, 2004.

[7] K.S. Krane, "Introductory nuclear physics". Wiley, 1987.

[8] Y. Oganessian, "Heaviest nuclei from ^{48}Ca-induced reactions", *Journal of Physics G: Nuclear and Particle Physics*, vol. 34, no. 4, pp. 165–242, 2007.

[9] N. Angert, "Ion beams at GSI", *International Journal of Radiation Applications and Instrumentation. Part D. Nuclear Tracks and Radiation Measurements*, vol. 19, no. 1-4, pp. 871 – 874, 1991.

[10] `http://www-inj.gsi.de/content/extern/pictures/content/overview.png`, October 2011.

[11] K. Eberhardt et al., "Preparation of targets for the gas-filled recoil separator TASCA by electrochemical deposition and design of the TASCA target wheel assembly", *Nuclear Instruments and Methods in Physics Research Section A: Accelerators, Spectrometers, Detectors and Associated Equipment*, vol. 590, no. 1-3, pp. 134 – 140, 2008.

[12] M. Leino, "In-flight separation with gas-filled systems", *Nuclear Instruments and Methods in Physics Research Section B: Beam Interactions with Materials and Atoms*, vol. 126, no. 1-4, pp. 320 – 328, 1997.

[13] H.D. Betz, "Charge states and charge-changing cross sections of fast heavy ions penetrating through gaseous and solid media", *Reviews of Modern Physics*, vol. 44, no. 3, p. 465, 1972.

[14] M. Schädel, D. Ackermann, and A. Semchenkov, "The TASCA Project", GSI Annual Report, GSI, 2005.

[15] `http://www-win.gsi.de/tasca/photo_gallery/birth_of_tasca/16_09_05.jpg`, November 2011.

[16] A. Semchenkov et al., "The TransActinide Separator and Chemistry Apparatus (TASCA) at GSI - Optimization of ion-optical structures and magnet designs", *Nuclear Instruments and Methods in Physics Research Section B: Beam Interactions with Materials and Atoms*, vol. 266, no. 19-20, pp. 4153 – 4161, 2008.

[17] L.-L. Andersson et al., "TASISpec - A highly efficient multi-coincidence spectrometer for nuclear structure investigations of the heaviest nuclei", *Nuclear Instruments and Methods in Physics Research Section A: Accelerators, Spectrometers, Detectors and Associated Equipment*, vol. 622, no. 1, pp. 164 – 170, 2010.

[18] U. Forsberg, "Pulse Shape Analysis for Heavy Element Spectroscopy", Master's thesis, Lund University, 2010.

[19] U. Forsberg et al., "Pulse Shape Analysis for the TASISpec Implantation Detector." GSI Annual Report, 2010.

[20] H.G. Essel et al., "The new data acquisition system at GSI", *IEEE Transactions on Nuclear Science*, vol. 43, p. 132, 1996.

[21] H.G. Essel and N. Kurz, "The general purpose data acquisition system MBS", *Real Time Conference, 1999.*, pp. 475–478, 1999.

[22] `http://www.srim.org/`.

[23] R.B. Firestone and V.S. Shirley, "Table of Isotopes, Volume 2, 1998 Update". John Wiley & Sons, 1998.